Interface structure and film polarization in epitaxial SrTiO_{3}/Si(001)

A. M. Kolpak and S. Ismail-Beigi

Phys. Rev. B **85**, 195318 — Published 18 May 2012

DOI: 10.1103/PhysRevB.85.195318

Interface structure and film polarization in epitaxial $SrTiO_3$/Si(001)

A. M. Kolpak and S. Ismail-Beigi
Center for Research on Interface Structures and Phenomena and Department of Applied Physics, Yale University, New Haven, CT 06520-8284

Phenomenological models suggest that thin epitaxial $SrTiO_3$ films on silicon will exhibit ferroelectric behavior as a result of compressive strain. However, such models do not include atomic-scale interface effects, which can dramatically alter the predicted behavior. In this paper, we use density functional theory computations to systematically elucidate the effects of the interface atomic structure and composition on the properties of $SrTiO_3$/Si heterostructures. We show that while the band alignment and metallicity of the heterostructure are highly sensitive to the chemical composition and geometry of the interface, the system also exhibits several important features that are universal to all compositions. These universal features, which include an electronic dipole across the interface and a large cation-oxygen displacement in the interfacial oxide layer, conspire to induce a net positive polarization in ultrathin $SrTiO_3$ films. We demonstrate that, due to its origin in the chemical bonds at the interface, this polarization is pinned in a single direction. Our results provide a fundamental understanding of the important role played by interfacial chemical bonds within the general class of atomically abrupt, oxide-semiconductor heterostructures and, furthermore, suggest guidelines for the future design of coupled functional oxide-semiconductor devices.

PACS numbers:

I. INTRODUCTION

Developing a fundamental understanding of the atomic scale chemical and physical interactions that characterize complex oxide-semiconductor interfaces and being able to predict the effects of these interactions at larger length scales could potentially have important consequences for applications in electronics, energy storage and harvesting, and nanotechnology. These are challenging goals, as even describing the atomic structure of a heterointerface is often a problem in a multidimensional phase space of chemical composition, geometry, and morphology. However, one can potentially narrow this phase space by determining the fundamental chemical/physical principles driving the interface formation in a prototype example. Here, we show that one can use the epitaxial $SrTiO_3$/Si interface as a model system to map out the relationships between the interface composition, the atomic and electronic structure, and the functional properties of the general class of complex oxide-semiconductor heterostructures.

The $SrTiO_3$/Si system is of interest in its own right as a potential building block to integrate the functional properties of oxides into established semiconductor technologies. We showed previously[1] that the interface plays an important role in determining the properties of the $SrTiO_3$/Si system, stabilizing a polarization despite thin film effects and inhibiting ferroelectric switching. Elucidating the mechanism for ferroelectric inhibition in $SrTiO_3$/Si can guide attempts to engineer an interface that successfully couples the ferroelectric polarization of complex oxides with charge carriers in industrially important semiconductor substrates; such an interface could lead to ferroelectric field effect transistors and other novel devices. In addition, understanding the phenomenon of interface-induced polarization may lead to the design of systems with novel physical properties that could be used for a wide range of applications, such as photovoltaics, ultra-low power devices, and heterogeneous catalysis.

In Ref.[1], we reported that the interface-induced polarization and lack of ferroelectricity observed in the experimentally realized $SrTiO_3$/Si heterostructure is ubiquitous to all $SrTiO_3$/Si interface compositions. The aim of this paper is to explore this universality in more detail, as well as to provide course-grained models incorporating the key physics. We focus on the behavioral trends in the atomic and electronic properties due to the most experimentally relevant perturbations of the interface composition: variation of the interfacial oxygen and strontium concentrations, the identity of the first oxide layer (SrO or TiO_2), and the type of cations in the interface region.

To date, the successful growth of epitaxial $SrTiO_3$ on silicon requires the use of layer-by-layer growth methods such as molecular beam epitaxy (MBE) and pulsed layer deposition (PLD) to obtain an atomically abrupt interface without the presence of an SiO_2 region[1–4]. Experiments indicate that such methods result in the presence of a significant concentration ($\sim 10^{18} cm^{-3}$) of oxygen vacancies in the $SrTiO_3$[5]. As oxygen vacancies have been shown to stabilize a negatively poled state in ultrathin perovskite films[6], they could play a key role in determining the functional properties of the $SrTiO_3$/Si heterostructure[7]. Furthermore, it has been suggested that small differences in the oxygen partial pressure during growth may yield different $SrTiO_3$/Si interface structures and thus properties[4], making it essential to understand the role of oxygen in this system.

Epitaxial growth of $SrTiO_3$/Si also requires the initial deposition of half a monolayer (ML) of Sr atoms[2,3], which nominally compensate the dangling bonds at the dimerized surface of the silicon substrate[8,9] and prevent the formation

of an amorphous SiO_2 layer at the $SrTiO_3$/Si interface. Additional Sr is then deposited to begin the growth of the $SrTiO_3$(001) film with a SrO layer. The initially proposed $SrTiO_3$/Si interface structure[2], as well as a number of other suggestions[9–11], thus include an interface buffer layer composed of 1/2 ML of Sr and varying amounts of oxygen between the Si and a SrO-terminated $SrTiO_3$ film. However, TEM images of the system indicate the presence of a full ML of Sr at the interface[1,3,4], and our recent first-principles based thermodynamic and kinetic analysis of the growth procedure also predicts the formation of a heterostructure with a full ML of Sr[12]. Again, possible differences in the growth procedure may lead to structures with different interfacial Sr compositions. Therefore, an understanding of how the Sr concentration affects the heterostructure properties is relevant.

Although the currently implemented growth procedures suggest that the initial atomic layer of the $SrTiO_3$ film is composed of SrO, several TEM studies[1,3,4] find that the $SrTiO_3$ plane adjacent to the interface is composed of TiO_2. Therefore, we examine the properties of heterostructures with both possible initial $SrTiO_3$ atomic layers. In addition, we discuss the properties of Ti- and Si-rich interface phases. The latter have been proposed to fit experimental data[2], but the former are relatively unexamined as the growth conditions are typically Sr-rich. Nevertheless, due to the relatively high temperatures during the film growth, considerable atomic diffusion can be expected to occur, making it possible for Ti to end up adjacent to the silicon substrate. Furthermore, examining the behavior of different cations at the interface can lead to a deeper fundamental understanding of the physical and chemical properties that govern the heterostructure behavior.

Our results show that the electronic properties of the $SrTiO_3$/Si heterostructure are quite sensitive to the interface composition, exhibiting large changes in the band alignment across the interface, as well as variations from insulating to quasi-2D metallic behavior. At the same time, we demonstrate that the all members of the general class of $SrTiO_3$/Si interfaces share several universal features, most importantly a significant cation-oxygen displacement in the oxide layer adjacent to the interface and an electronic interface dipole oriented towards the silicon substrate, both of which act to pin the polarization direction. In this paper, we examine the origin of these universal interfacial boundary conditions and their effects on the functional properties of $SrTiO_3$/Si, and furthermore, we show that both the boundary conditions and their consequences are in fact general characteristics of perovskite oxide/semiconductor interfaces.

The remainder of the paper is structured as follows. After describing our methods in Section II, we provide an overview of the compositions of the $SrTiO_3$/Si interface that we consider in Section III. In Section IV, we discuss the presence and origin of several composition-independent (universal) properties. We examine the composition-dependent properties in Section V. In Section VI, we present data on the ferroelectric behavior of strained $SrTiO_3$ thin films, demonstrating that a strong coupling between the $SrTiO_3$/Si interface and the functional properties of the oxide stabilizes a single monodomain polar state and prevents ferroelectric switching. We develop a phenomenological model to describe the coupling between the interface and the film polarization in Section VII. We further generalize our results to other ferroelectric oxide/semiconductor interfaces in Section VIII. Finally, we conclude in Section IX.

II. METHODS

DFT calculations are performed within the generalized gradient approximation (GGA) using the dacapo code[13] and ultrasoft pseudopotentials[14] with a 30 Ry cutoff energy. An example simulation supercell is shown in Fig. 1. Supercells are composed of a 13 atomic layer-thick Si substrate with (001) surfaces, an interfacial layer, and 3 to 11 unit cells of $SrTiO_3$. The vacuum-exposed Si surface is passivated with hydrogen atoms in order to facilitate the simulation of a thick Si substrate. The $SrTiO_3$ film is terminated with a SrO plane, and this surface is capped by a metal electrode or directly exposed to vacuum (see below): in Fig. 1 gold is used; in general, a metallic electrode provides an electron reservoir for the system. The electronic and structural properties of the slabs are well converged with respect to both the Si and electrode thickness in addition to the k-point sampling ($8\times8\times1$ Monkhorst-Pack per 1×1 surface unit cell) and Fermi temperature (0.05 eV). Periodic copies of the supercell are separated by $\approx$12 Å in the z-direction (perpendicular to the interface). A dipole correction[15] is included in the middle of the vacuum to prevent spurious electrostatic interactions. The in-plane lattice constant is fixed to the theoretical Si lattice constant (a=3.866 Å), resulting in a 1.7% compressive strain on the $SrTiO_3$, which corresponds to the experimental strain at room temperature[16]. For each interface composition, we perform relaxations from ferroelectric configurations with initial imposed bulk displacements in the $SrTiO_3$ oriented towards and away from the silicon substrate, as well as from an initial paraelectric configuration. All atoms are relaxed completely until the forces on each atom have magnitudes < 0.01 eV/Å along all axial directions.

The interfacial layer, which is defined as the atomic plane adjacent to both a full atomic layer of silicon and a full atomic layer of $SrTiO_3$, is varied by changing the number of Sr, Ti, Si, and O atoms. The initial $SrTiO_3$ plane is also varied, so that structures in which the interface layer is in contact with either a SrO or a TiO_2 plane are considered. In addition, the relaxed structures and total energies of several possible registries between the film and the silicon

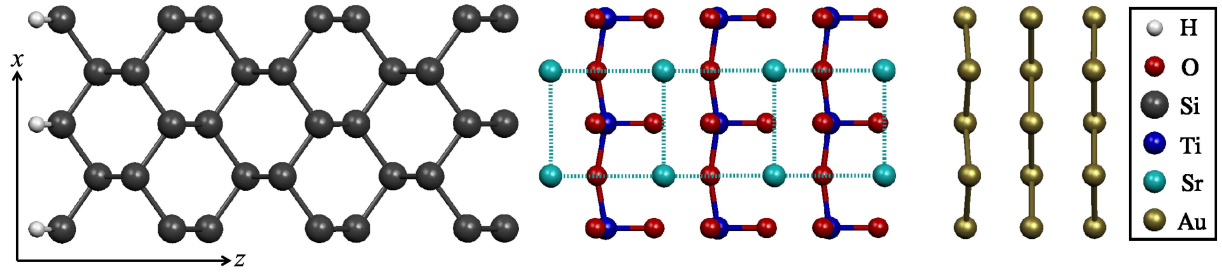

FIG. 1: Example of a simulation supercell with a top electrode, showing the relaxed atomic structure of the experimentally realized interface composition. The silicon surface is passivated with H in the calculation to facilitate simulation of a thick silicon substrate. The Au electrode provides an electron reservoir; computations are performed both with and without such a reservoir.

substrate are computed for each composition; below, only the lowest energy structure for each composition is discussed. The interface compositions studied include but are not limited to the previously proposed structures[9–11,17–21], for a total of 56 compositions. A representative subset of these structures can be found in Figs. 2-5, as well as in the supplementary material of Ref.[1].

Experimental measurements provide evidence for both (2×1) and (1×1) in-plane symmetry; therefore the in-plane symmetry of the supercell is (2×1) for most calculations, allowing for the formation of Si dimers at the interface, as well as consideration of a large variety of compositions. In some cases, additional calculations were performed with (n×1) symmetry where n=3,4,5. Tests with c(2×2) in-plane symmetry, which were performed for several interface compositions, show no evidence for octahedral rotations or tilting patterns in the $SrTiO_3$ film that cannot be encompassed within the basic (2×1) supercell.

For several interface compositions, we also perform GGA+U calculations within the rotational invariant approach[22]. A range of U values is applied separately to either the Ti d-states or the Si p-states to investigate the sensitivity of the interfacial electronic structure (*e.g.*, the band alignment and the presence or absence of Fermi level pinning) to the details of the exchange-correlation model (Section V B).

III. INTERFACE STRUCTURES AND COMPOSITIONS

In this section, we introduce a representative subset of the $SrTiO_3$/Si interface compositions that we have investigated. The minimum energy atomic geometries computed for these compositions are illustrated in Figs. 2-5. (We analyzed the thermodynamic and kinetic stability of these compositions in Ref.[12].) We examine the structural changes in the interface region with respect to four types of perturbation: i) variation in the interfacial O concentration; ii) change in the interfacial Sr composition; iii) change in the identity of the $SrTiO_3$ atomic plane adjacent to the interface (SrO or TiO_2); and iv) substitution of the interfacial Sr with Si and/or Ti cations. In particular, we examine composition-induced changes to the average silicon-oxide separation (*i.e.*, the thickness of the interface layer), the length of the Si dimer bonds, and the cation-oxygen displacements in the $SrTiO_3$ layer adjacent to the interface. Knowledge of the variation in these parameters with respect to composition can be used in conjunction with experimental data to determine the interface atomic geometry and composition of actual fabricated heterostructures[23].

Figures 2a-c show variations of the composition that would be expected, assuming no atomic rearrangements, based on the layer-by-layer growth procedure from Refs.[24]. In Fig. 2a, the interface layer (IFL) consists of half a monolayer (ML) of Sr atoms in an ordered 2×1 stripe pattern on the dimerized Si(001) surface. The atomic plane of the $SrTiO_3$ adjacent to the interface (the first oxide layer, or FOL) is composed of SrO. Due to possible differences in the oxygen partial pressure and/or the deposition rate, the oxygen content of the IFL may vary. In Fig. 2b, a full ML of oxygen (one oxygen per Si atom) is added to the IFL from Fig. 2a; an additional 1/2 ML of oxygen is inserted into the IFL to form the structure shown in Fig. 2c.

As Fig. 2 shows, the structural changes due to the increasing oxygen content are relatively minor, consisting primarily of an increase in the average distance between the silicon and the FOL and a decrease in the average cation-oxygen displacement within the FOL. The silicon dimer bond length also increases significantly for the structure with 3/2 ML oxygen in the interface, as an oxygen is inserted into the dimer bond. Any further increase in the oxygen composition requires the formation of a distinct SiO_2 interfacial layer, which is not observed experimentally and is not considered here. The computed distances are compiled in Table I, which also describes the nomenclature used to refer to the different interface compositions in the remainder of this work.

Also shown in Fig. 2 are structures with a full ML of Sr in the IFL. To obtain 1 ML Sr at the interface requires

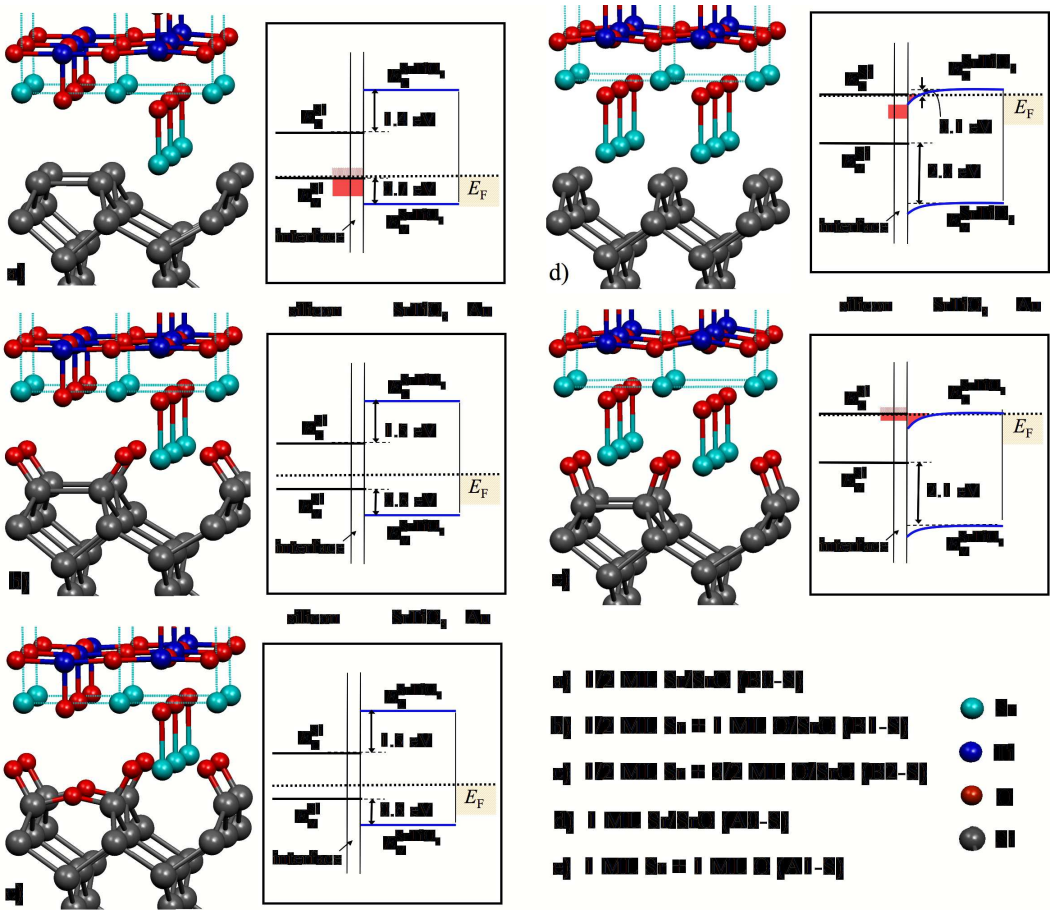

FIG. 2: Relaxed atomic structures and schematics of the computed band alignment for various interface compositions with a Sr-based interface layer and a first oxide layer composed of SrO. Oxygen concentration increases from top to bottom; Sr concentration increases from left to right. The band diagrams also indicate the energetic range and spatial position of interface states (shaded red areas), and are discussed in Sec. V A. The naming convention (in parentheses) connects the structures to the properties reported in Tables I-III.

atomic rearrangements during the film growth. This is consistent with the relatively high temperatures used in the growth procedure; furthermore, STEM images of $SrTiO_3$/Si heterostructures indicate a full ML of Sr adjacent to the top silicon layer[1,3,4]. As shown in the Table, the 1 ML Sr compositions exhibit the same trend as the 1/2 ML Sr compositions with respect to the average distance between the silicon and the oxide. Interestingly, however, the Si dimers are absent in the lowest energy structure shown in Fig. 2d, which has 1 ML of Sr and no oxygen in the IFL, resulting in a 1×1 in-plane symmetry; addition of oxygen to the IFL restores the 2×1 Si dimer structure (Fig. 2e).

Figure 3 illustrates the atomic structure of heterostructures with the same IFL as those shown in Fig. 2, but with the FOL composed of TiO_2 instead of SrO. These compositions exhibit the same trends with respect to oxygen and Sr concentration in the IFL as those with a SrO FOL. However, in general, compositions with a TiO_2 layer adjacent to the interface are characterized by a shorter average silicon-oxide distance. In addition, the $SrTiO_3$ registry with respect to the underlying silicon substrate shifts by half a unit cell. As a result, the interfacial Sr atoms are located in continuation of the perovskite lattice. As we discuss later, the shorter silicon-oxide distance observed in compositions with a TiO_2 FOL increases the stability of the heterostructure and also has significant effects on the electronic structure.

Despite the fact that the growth procedures begin with Sr deposition onto the silicon surface, there is no reason *a priori* that the interface layer must be Sr-based; the temperature is sufficiently high during the growth that rearrangement to yield a Ti-based IFL is feasible. Figure 4 illustrates a number of possible Ti-based interface compositions. Due to the higher oxidation state of Ti, it is possible to include more oxygen in Ti-based IFLs compared to their Sr-based counterparts, as indicated by the data in Table I. Nevertheless, these structures exhibit similar trends with respect to the interface cation and oxygen concentrations. The FOL for all of the compositions in Fig. 4 is SrO. We have also computed the ground state structures of analogues with a TiO_2 FOL (not shown). As with Sr-based IFL

TABLE I: Key parameters of computed interface geometries: cation-oxygen displacement in the $SrTiO_3$ layer adjacent to the interface ($\delta z_{\rm int}$) in Å; z-distance between the interfacial Sr (or Ti) and oxygen in the first oxide layer ($d_{\rm Sr(Ti)-O}$) in Å; average z-distance between the top silicon layer and the first oxide atomic plane ($d_{\rm Si-oxide}$) in Å; silicon dimer length (l_{dimer}) in Å. IFL: interface layer, FOL: first oxide layer

label	IFL	FOL	$\delta z_{\rm int}$	$d_{\rm Sr(Ti)-O}$	$d_{\rm Si-oxide}$	$l_{\rm dimer}$
A0-S	1 ML Sr	SrO	0.47	2.32	4.03	no dimer
A1-S	1 ML Sr + 1 ML O	SrO	0.60	2.27	4.58	2.50
C0-S	$\frac{1}{2}$ ML Sr + $\frac{1}{2}$ ML Si	SrO	0.50	2.36	3.41	2.55
B0-S	$\frac{1}{2}$ ML Sr	SrO	0.26	2.25	3.52	2.53
B1-S	$\frac{1}{2}$ ML Sr + 1 ML O	SrO	0.18	2.32	3.87	2.52
B2-S	$\frac{1}{2}$ ML Sr + $\frac{3}{2}$ ML O	SrO	0.15	2.31	3.99	3.19
A0-T	1 ML Sr	TiO_2	0.35	1.68	3.56	no dimer
A1-T	1 ML Sr + 1 ML O	TiO_2	0.25	1.64	3.99	2.51
C0-T	$\frac{1}{2}$ ML Sr + $\frac{1}{2}$ ML Si	TiO_2	0.28	1.61	3.49	2.54
B0-T	$\frac{1}{2}$ ML Sr	TiO_2	0.24	1.60	3.33	2.44
B1-T	$\frac{1}{2}$ ML Sr + 1 ML O	TiO_2	0.10	1.70	3.64	2.48
B2-T	$\frac{1}{2}$ ML Sr + $\frac{3}{2}$ ML O	TiO_2	0.10	1.70	3.76	3.23
D0-S	1 ML Ti	SrO	0.65	1.80	2.79	no dimer
D1-S	1 ML Ti + 1 ML O	SrO	0.67	1.78	3.23	3.06
D2-S	1 ML Ti + $\frac{3}{2}$ ML O	SrO	0.66	1.77	3.57	3.28
D3-S	1 ML Ti + 2 ML O	SrO	0.25	1.94	3.89	no dimer
F0-S	$\frac{1}{2}$ ML Ti + $\frac{1}{2}$ ML Si	SrO	0.65	1.81	2.77	no dimer
E0-S	$\frac{1}{2}$ ML Ti	SrO	0.48	1.75	3.16	3.59
E1-S	$\frac{1}{2}$ ML Ti + 1 ML O	SrO	0.43	1.70	3.56	2.69
E2-S	$\frac{1}{2}$ ML Ti + $\frac{3}{2}$ ML O	SrO	0.40	1.70	3.66	3.13

compositions, switching the FOL from SrO to TiO_2 results in a decrease in the silicon-oxide separation. However, as we find that these Ti-rich structures are all unstable with respect to formation of bulk $TiSi_2$[12], which is not observed experimentally, and hence they are not further discussed here.

Replacing half the cations in the IFL of Figs. 2d, 3d, and 4d with Si yields the structures shown in Fig. 5. As the data in Table I shows, these compositions exhibit behavior similar to the structures with a full ML of cations in the IFL. We have also investigated a number of additional interface compositions, including those with smaller concentrations of Sr, O, and/or Ti in the IFL. However, as these compositions exhibit the structural and electronic behavior expected by extrapolating the trends from the subset of compositions discussed above, we do not explicitly discuss them here.

IV. UNIVERSAL INTERFACE PROPERTIES

In this section, we discuss the properties universal to the interface between silicon and $SrTiO_3$. Resulting from fundamental chemical/physical interactions, these properties are manifest regardless of the interface composition and have significant implications for the functional behavior of the entire heterostructure (Section VI).

A. Electronic dipole

A key feature observed for all interface compositions is a redistribution of electrons from the silicon to the $SrTiO_3$ side of the interface, resulting in the formation of an electronic dipole. In brief, one would expect such a redistribution on basic chemical grounds: oxygen is the most electronegative element in the heterostructure so one can expect that electrons will always transfer from the more electropositive Si and Sr interfacial atoms to the oxygen atoms of the FOL. (A somewhat more detailed discussion can be found in Ref.[1].)

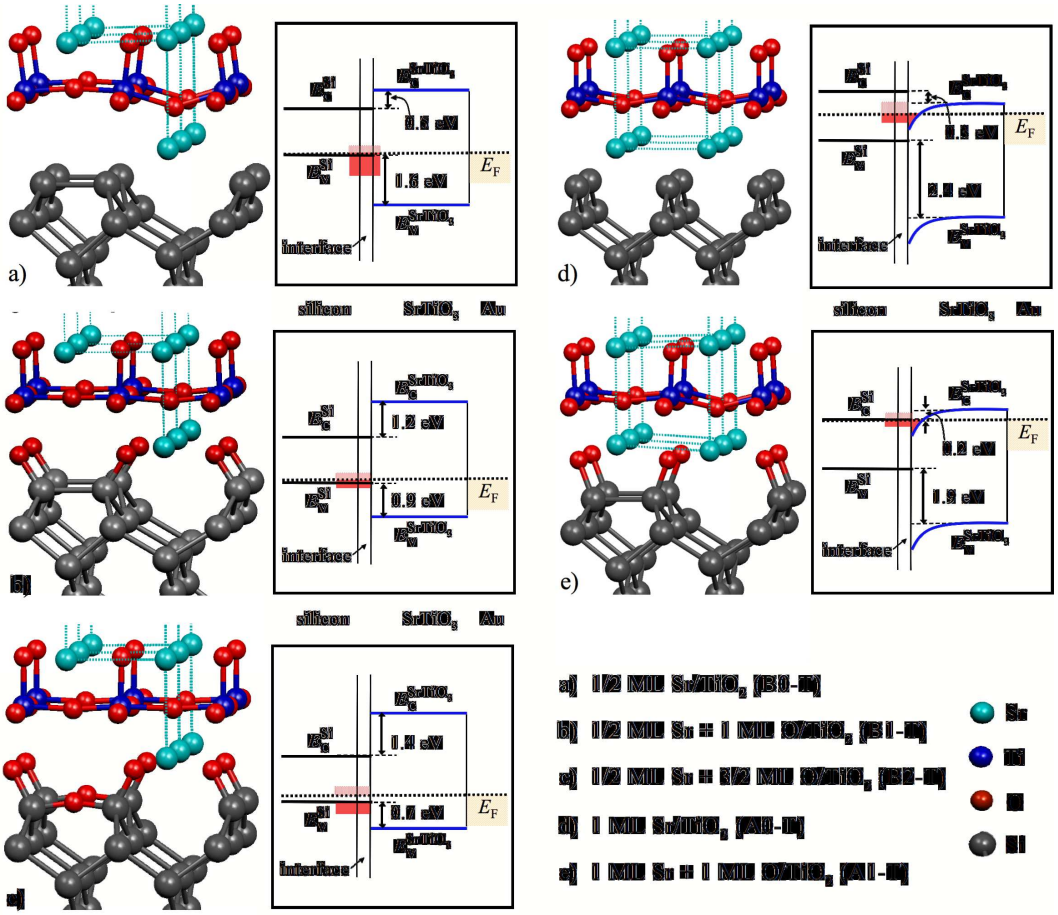

FIG. 3: Relaxed atomic structures and schematics of the computed band alignment for various interface compositions with a Sr-based interface layer and a first oxide layer composed of TiO_2. Oxygen concentration increases from top to bottom; Sr concentration increases from left to right. The band diagrams also indicate the energetic range and spatial position of interface states (shaded red areas), discussed in Sec. V A.

This phenomenon can be seen clearly in Figs. 6 and 7, which show the induced electron density — the electron rearrangement due to the formation of the interface — for various interface compositions. The induced electron density $\delta\rho(x, y, z)$ is determined directly from first-principles computations:

$$\delta\rho(x, y, z) = \rho_{\text{total}}(x, y, z) - \rho_{\text{Si/Sr}_x\text{O}_y}(x, y, z) - \rho_{\text{SrTiO}_3}(x, y, z), \tag{1}$$

where ρ_{total} is the computed electronic charge density of the actual $\text{Si/Sr}_x\text{O}_y\text{/SrTiO}_3$ heterostructure, and $\rho_{\text{Si/Sr}_x\text{O}_y}$ and ρ_{SrTiO_3} are the electronic charge densities of separated $\text{Si/Sr}_x\text{O}_y$ slab and $SrTiO_3$ slabs, respectively. (The latter charge densities are computed using the fixed atomic geometries taken from the $\text{Si/Sr}_x\text{O}_y\text{/SrTiO}_3$ system.) The plots in Figs. 6 and 7 show the induced electron density integrated in the direction perpendicular to the page $\delta\rho(x, z) = \int_y \delta\rho(x, y, z)dy$.

We note that, in principle, the choice of dividing plane is arbitrary. However, in our case an examination of the densities of states shows electron transfer between different atomic orbitals which helps identify that this particular division produces the simplest physical picture. For example, the densities of states indicate electron transfer from the Si/Sr layers and into the Ti *d*-orbitals in the TiO_2 layer closest to the Si/Sr: see the density of states in Figs. 9 and 10, and the schematic band diagrams in Figs. 3–5.

Figure 6 shows $\delta\rho(x, z)$ for heterostructures in which the first oxide layer is composed of SrO. For each composition, $\delta\rho$ is clearly dominated by ionic bonding between the Sr cations in the IFL and the oxygen anions directly above them in the FOL. The strength of this interaction is illustrated by the intense region of electron loss (red/magenta) directly above each interfacial Sr cation and the corresponding region of electron gain (blue/cyan) directly below the oxygen anions.

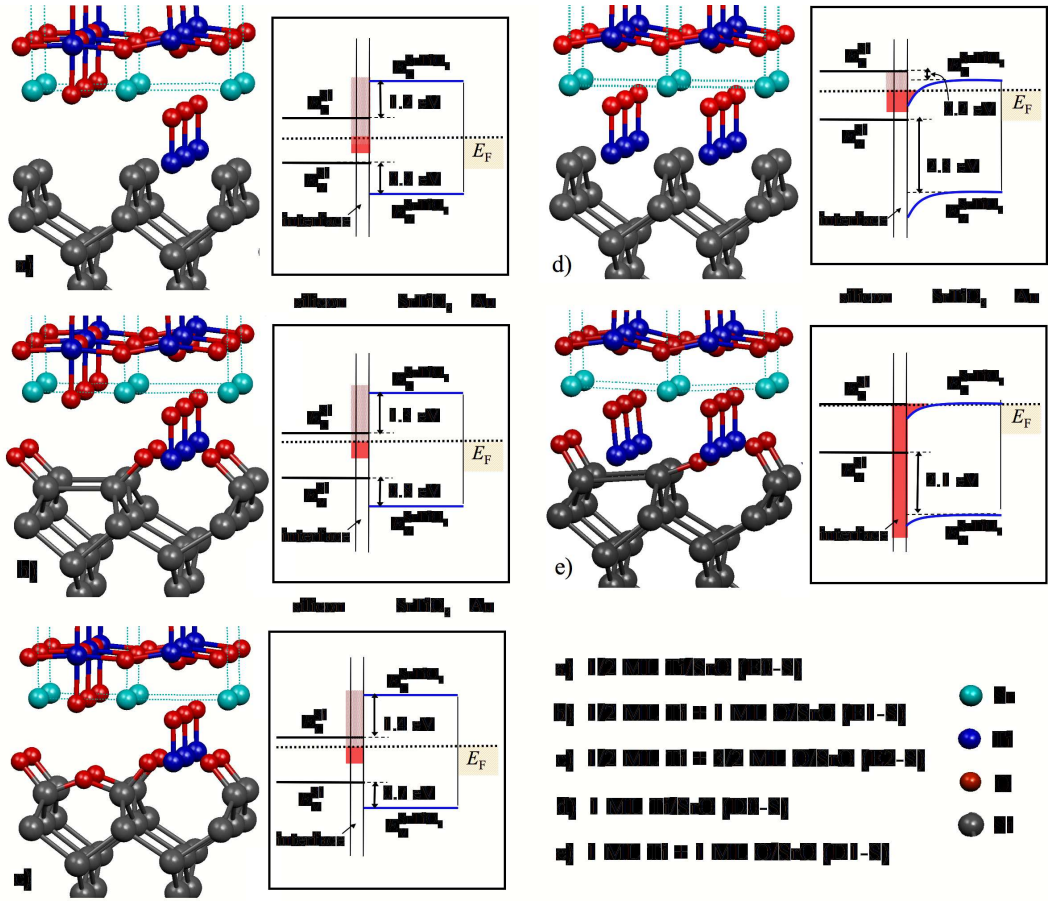

FIG. 4: Relaxed atomic structures and schematics of the computed band alignment for compositions with a Ti-based interface layer. The band diagrams also indicate the energetic range and spatial position of interface states (shaded red areas), discussed in Sec. V A.

The induced electron density plots for heterostructures with a TiO_2 layer adjacent to the interface, shown in Fig. 7, show a qualitatively similar electron rearrangement, with electrons moving from the IFL to the FOL. Due to the perovskite-like geometry of the interface cations with respect to the FOL, the Sr-O bonds across the interface are along the (111) direction, instead of perpendicular to the interface as is the case for the compositions in Fig. 6. In addition, each interfacial Sr bonds to two oxygens in the TiO_2 FOL. Consequently, there is a gain in electron density in the oxygen p_x and p_y orbitals that overlap with the interfacial Sr (and a loss of charge density from the Si/Sr hybrid orbitals), leading to the characteristic charge redistribution seen in Fig. 7. Figure 8 illustrates this distribution in the plane of the interface, which shows the induced charge density (integrated perpendicular to the interface) for the composition with 1 ML Sr in the IFL (Fig. 7d).

As expected, all the panels in Figs. 6 and 7 indicate that the interfacial bonding is primarily ionic in nature: in general, the electrons redistribute away from Si/Sr and towards the FOL. In contrast, in a predominantly covalent bonding mode, electrons would move away from both the Si/Sr and FOL towards the space between the two. As the figures show, such a redistribution is not observed here: in all the panels we see intense electron loss (red region) in the space between the Si/Sr and the FOL.

In addition to the ionic bonding between the cations in the IFL and the oxygens in the FOL, the induced electron density also reveals various other chemical interactions in the interfacial region. For example, compositions including oxygen in the IFL (*e.g.*, panels b, c, and e in Figs. 6 and 7) exhibit distinct dipoles in alternating directions as one moves parallel to the interface.

We quantitatively determine the sign and magnitude of the net interface dipole moment per surface 1×1 unit cell from the induced electron density:

$$p_{\text{int}} = \int_1^2 \delta\rho(z) z dz, \tag{2}$$

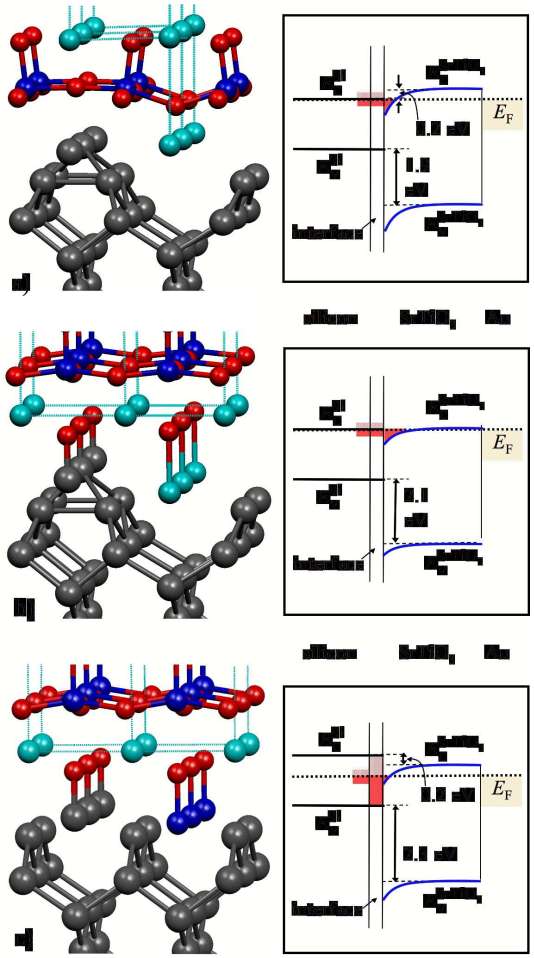

FIG. 5: Relaxed atomic structures and schematics of the computed band alignment for Si-rich interface compositions: a) C0-T, b) C0-S, and c) F0-S. Si, Sr, Ti, and O atoms are grey, cyan, blue, and red spheres, respectively. The band diagrams also indicate the energetic range and spatial position of interface states (shaded red areas), discussed in Sec. V A.

where $\delta\rho(z)$ is the average induced electron density perpendicular to the interface, and the integration is from the bulk-like region on the silicon side of the interface where $\delta\rho(z) \rightarrow 0$ to the region on the $SrTiO_3$ side of the interface, where $\delta\rho(z) \rightarrow 0$ again. The computed values of $p_{\rm int}$ are provided in Table II.

Table II shows that for a given FOL, the magnitude of the interface dipole increases with the concentration of Sr cations and decreases with the concentration of O anions in the IFL, suggesting that $p_{\rm int}$ is directly related to the polarization of the bonds between ions in the interface layer and those in the FOL. For compositions including oxygen in the IFL, bonds between interface O anions and Sr cations in the FOL contribute dipoles in the opposite direction to bonds between interface Sr cations and O anions in the FOL. However, because the oxygens in the interfacial layer also form strong bonds to the silicon substrate, the former bonds are weaker, as indicated by the longer bond distances and less intense regions of electron rearrangement in Fig. 6. Consequently, the net dipole is always oriented along the bonds between the interface cations and the oxygens in the FOL (*i.e.*, towards the silicon substrate). As described previously[1], this fixed dipole direction is driven by the lowering of the Madelung potential and restitution of a bulk-like environment for the highly electronegative oxygen in the FOL.

The data in Table II and Figs. 6 and 7 suggest that, in principle, one could switch the direction of the interface dipole moment by further increasing the oxygen content or decreasing the Sr content of the interface. In practice, it is not possible to increase the former sufficiently to switch the interface dipole, primarily as a result of structural and thermodynamic constraints. Our calculations show that more oxygen simply does not fit into the interface layer, instead intercalating into the Si substrate, leading to the formation of an amorphous SiO_2 region. In an amorphous interface, one would expect the net (SiO_2/$SrTiO_3$) interface dipole to disappear, although similar phenomena to those discussed above would be observed locally. In addition, the coherent cation-oxygen displacements observed in the abrupt interfaces would no longer exist, and the $SrTiO_3$ film would no longer be compressively strained. Decreasing

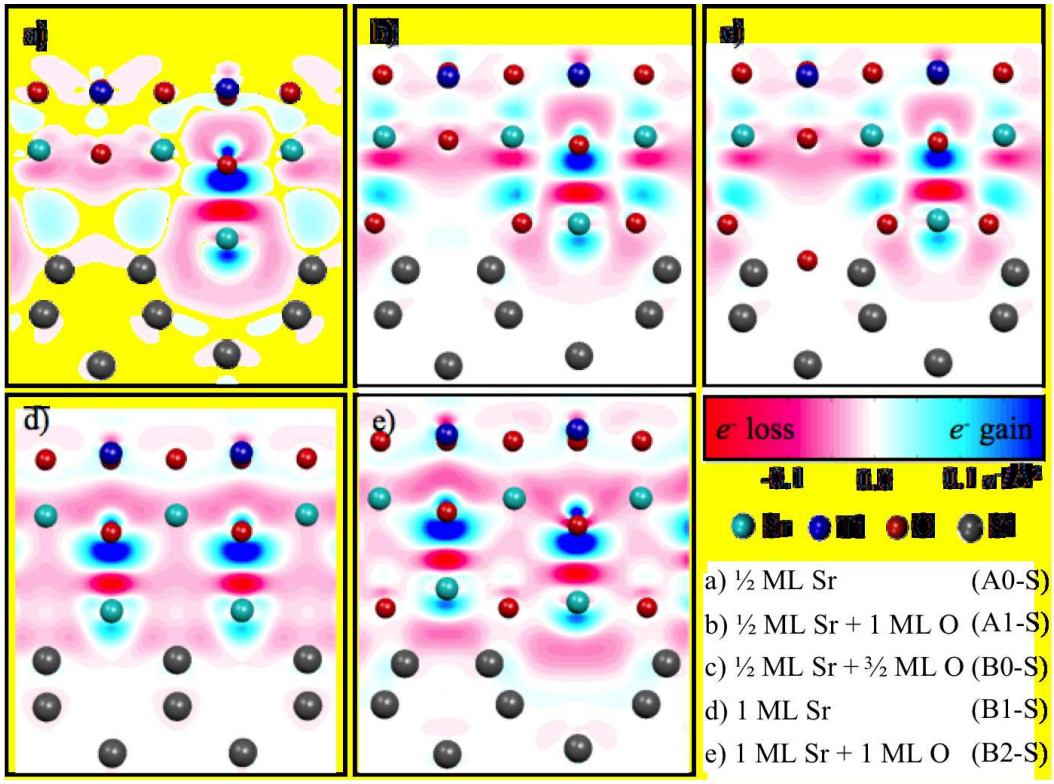

FIG. 6: Electron rearrangement in the xz-plane (averaged over y) due to interface formation for compositions with a SrO plane adjacent to the interface layer. The interfacial oxygen concentration increases from left to right and the interfacial Sr concentration increases from top to bottom. Red and blue contours indicate electron loss and gain, respectively. Atom positions are indicated by the superimposed spheres.

the cation concentration of the interface layer results in excess interfacial oxygen, which then bonds more strongly with the silicon substrate, leading to a similar scenario.

B. Cation-oxygen displacement

The second universal feature observed for all interface compositions is a large, positive cation-oxygen displacement, or polarization, in the FOL. We use the convention that a positive (negative) polarization is oriented away from (towards) the silicon substrate. The computed value of the interfacial cation-oxygen displacement, denoted by $\delta z_{\rm int}$, is given for each composition in Table I; these displacements are visible in the atomic structure figures (Figs. 2—5). While the magnitude of $\delta z_{\rm int}$ varies with interface composition, its direction does not. This is a consequence of the interfacial electron rearrangement discussed in the previous section. In each case, the cations (anions) in the FOL are repelled (attracted) by the net positively charged Si/Sr interface region, causing them to displace away from (towards) the Si substrate.

As indicated by the data in Table II, there is a roughly a monotonic relation between $\delta z_{\rm int}$ and $p_{\rm int}$ for a given FOL; however, the relationship is difficult to quantify because the relevant bond distances change with the structure/composition of the interface. In addition, the bond distance and the amount of charge associated with each bond dipole do not vary independently. Nevertheless, there is a clear overall trend, with the magnitude of $\delta z_{\rm int}$ increasing with $p_{\rm int}$.

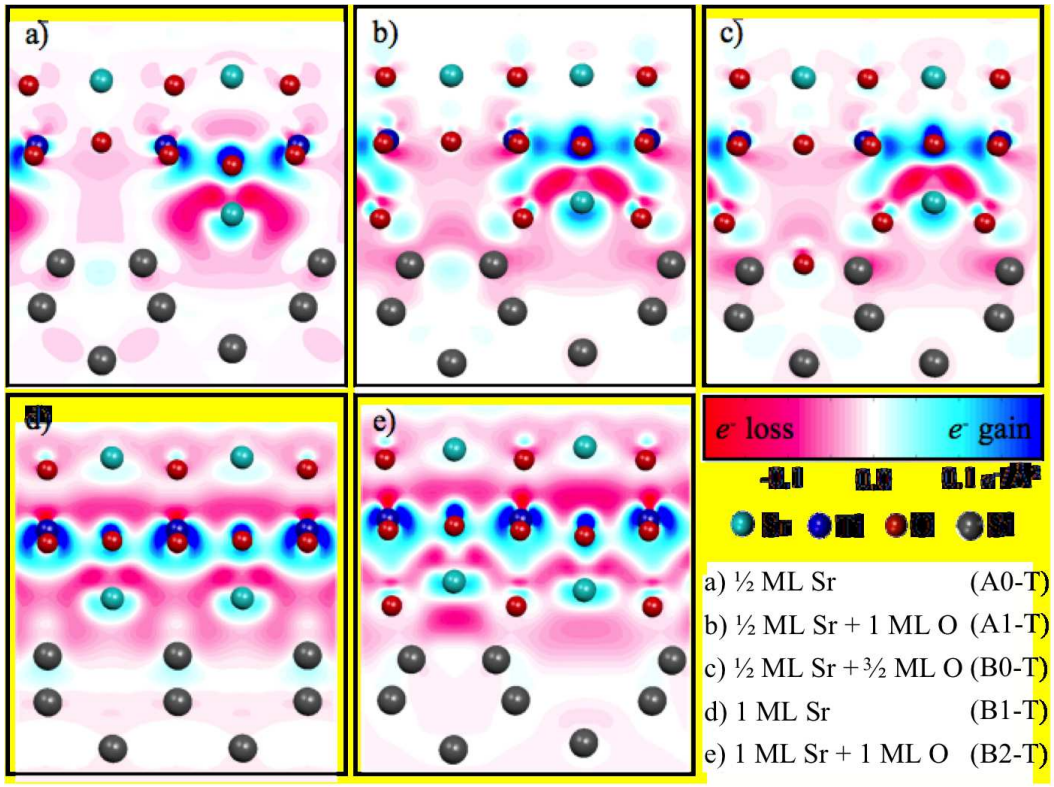

FIG. 7: Electron rearrangement in the xz-plane (averaged over y) due to interface formation for compositions with a TiO_2 plane adjacent to the interface layer. The interfacial oxygen concentration increases from left to right and the interfacial Sr concentration increases from top to bottom. Red and blue contours indicate electron loss and gain, respectively. Atom positions are indicated by the superimposed spheres.

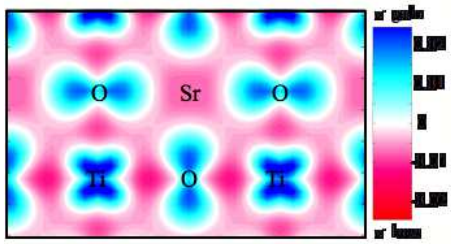

FIG. 8: Electron rearrangement due to interface formation in the plane parallel to the interface, illustrating the ionic bonding between an interfacial Sr cation and the two oxygen anions per 1×1 unit cell in the adjacent TiO_2 layer (*i.e.*, composition A0-T, Fig. 7d).

V. COMPOSITION-DEPENDENT INTERFACE PROPERTIES

A. Band alignment

One of the most important features governing the electronic properties of a heterostructure is the alignment of the valence and conduction bands across the interface between the two materials. In the simplest macroscopic picture of a semiconductor-semiconductor hetero-interface, the band alignment is determined by assuming a common vacuum level and taking the difference in the electron affinities of the two bulk materials[25]. In practice, this simple model is insufficient to predict the experimentally measured band offsets for as it does not include the effects of the interfacial chemistry which can induce additional electron redistribution and thus electronic potential offsets. Thus, first-principles computations are required if one wishes to predict the band offsets in a complex heterosystem and to understand how they are correlated to the atomic-level structural properties.

TABLE II: Computed interface dipole ($p_{\rm int}$), interface cation-oxygen displacement ($\delta z_{\rm int}$), and average cation-oxygen displacement over each atomic plane in the oxide film($\delta z_{\rm avg}$). Values of $p_{\rm int}$ are an average over the 2×1 interface supercell; values of $\delta z_{\rm avg}$ are for 3-unit-cell-thick films. u.c. refers to a 1×1 surface unit cell.

label	IFL	FOL	$p_{\rm int}$ (eÅ/u.c.)	$\delta z_{\rm int}$ (Å)	$\delta z_{\rm avg}$ (Å)
A0-S	1 ML Sr	SrO	0.28	0.47	0.24
A1-S	1 ML Sr + 1 ML O	SrO	0.25	0.60	0.31
C0-S	$\frac{1}{2}$ ML Sr + $\frac{1}{2}$ ML Si	SrO	0.15	0.50	0.29
B0-S	$\frac{1}{2}$ ML Sr	SrO	0.10	0.26	0.12
B1-S	$\frac{1}{2}$ ML Sr + 1 ML O	SrO	0.05	0.18	0.05
B2-S	$\frac{1}{2}$ ML Sr + $\frac{3}{2}$ ML O	SrO	0.04	0.15	0.04
A0-T	1 ML Sr	TiO_2	0.69	0.35	0.29
A1-T	1 ML Sr + 1 ML O	TiO_2	0.44	0.25	0.23
C0-T	$\frac{1}{2}$ ML Sr + $\frac{1}{2}$ ML Si	TiO_2	0.37	0.28	0.25
B0-T	$\frac{1}{2}$ ML Sr	TiO_2	0.37	0.24	0.21
B1-T	$\frac{1}{2}$ ML Sr + 1 ML O	TiO_2	0.31	0.10	0.09
B2-T	$\frac{1}{2}$ ML Sr + $\frac{3}{2}$ ML O	TiO_2	0.33	0.10	0.09
D0-S	1 ML Ti	SrO	0.14	0.65	0.36
D1-S	1 ML Ti + 1 ML O	SrO	0.28	0.67	0.41
D2-S	1 ML Ti + $\frac{3}{2}$ ML O	SrO	0.35	0.66	0.42
D3-S	1 ML Ti + 2 ML O	SrO	0.08	0.25	0.13
F0-S	$\frac{1}{2}$ ML Ti + $\frac{1}{2}$ ML Si	SrO	0.14	0.65	0.37
E0-S	$\frac{1}{2}$ ML Ti	SrO	0.20	0.48	0.27
E1-S	$\frac{1}{2}$ ML Ti + 1 ML O	SrO	0.25	0.43	0.26
E2-S	$\frac{1}{2}$ ML Ti + $\frac{3}{2}$ ML O	SrO	0.18	0.40	0.26

The computed band offsets for Au/$SrTiO_3$/Si heterostructures are shown schematically in Figs. 2—5 and compiled in Table III. The table shows that allowing for interface chemical bond formation leads to a larger valence band offset (and correspondingly smaller conduction band offset) compared to the reference system composed of separated silicon and $SrTiO_3$ slabs in the same supercell. In other words, there is always an additional potential energy drop for electrons across the interface due to chemical interactions. (See the Appendix for the details of the method used to compute the band offsets.)

As we employ DFT to compute the band structure, there are a number of possible shortcomings to the predicted band alignments. First, we need to account for the well-known underestimation of the band gap by DFT[26]. As explained in the Appendix, we empirically add rigid band shifts to reproduce the experimental band gaps for Si and $SrTiO_3$. Separately, our method assumes that DFT gives an accurate predictions of the valence band edges; however, it is known that more accurate treatments of the band edges can shift both conduction and valence bands from the DFT-predicted values (this is both seen in earlier work on the effect of the discontinuity of the DFT potential versus particle number[27] as well as more recent direct computations using more accurate non-local descriptions of exchange[28]). Obviously, more demanding computations (beyond the scope of this work) that use improved descriptions of exchange and correlation are needed to verify our predicted band alignments.

The band offsets compiled in Table III show that either adding oxygen or removing Sr from the IFL shifts the $SrTiO_3$ bands upwards with respect to the silicon compared to the interfaces with 1 ML of cations, although they remain significantly lower than the reference values. These observations suggest that the band offsets can be directly correlated to the density of bonds between the cations in the interface layer and the oxygen anions in the initial oxide layer. This supports the interpretation of the induced electron density plots in Section IV A which suggests that the interface dipole is primarily due to the polarization of the interfacial chemical bonds. For example, removing interfacial cations decreases the dipole density, while adding interfacial oxygens screens the dipole[10], both resulting in a smaller downwards shift in the $SrTiO_3$ potential compared to the 1 ML cation case.

We conclude our discussion of the band alignment in $SrTiO_3$/Si heterostructures by noting that several experimental measurements of the valence band offset have been reported. Using XPS, Amy *et al.* measure valence band offsets of 2.38 and 2.65 eV after annealing samples under high and low oxygen partial pressure, respectively[29]. Measurements of other samples give slightly smaller values of 2.1-2.2 eV, depending on the doping type of the silicon substrate[30,31].

TABLE III: Computed electronic structure properties for Au/$SrTiO_3$/Si heterostructures: valence band offset from Si to $SrTiO_3$(ΔE_V); conduction band offset from Si to $SrTiO_3$ (ΔE_C); density of states ± 0.1 eV around the Fermi level, excluding the electrode (DOS(E_F)); and spatial extent of the metallic region perpendicular to the interface, encompassing 95% of the states at the Fermi level (γ_{int}). The notation in parentheses indicates whether the Fermi level is close to the silicon valence or conduction band edge, VBE and CBE, respectively, or the Si mid-gap (MG). The reference supercell is a silicon slab separated by vacuum from a $SrTiO_3$ slab with SrO (reference supercell S) or TiO_2 (reference supercell T) surfaces, as discussed in the Appendix.

label	IFL	FOL	ΔE_V (eV)	ΔE_C (eV)	DOS(E_F) (states/2D cell)	γ_{int} (nm)
A0-S	1 ML Sr	SrO	-2.0	0.1*	0.09 (CBE)	0.9
A1-S	1 ML Sr, 1 ML O	SrO	-2.1	0.0*	0.06 (CBE)	1.7
C0-S	$\frac{1}{2}$ ML Sr, $\frac{1}{2}$ ML Si	SrO	-2.1	0.0*	0.11 (CBE)	1.1
B0-S	$\frac{1}{2}$ ML Sr	SrO	-0.7	1.4	0.08 (VBE)	1.2
B1-S	$\frac{1}{2}$ ML Sr, 1 ML O	SrO	-0.6	1.5	0.00 (MG)	insulating
B2-S	$\frac{1}{2}$ ML Sr, $\frac{3}{2}$ ML O	SrO	-0.6	1.5	0.00 (MG)	insulating
	reference supercell S	SrO	0.9	3.0	0.00 (VBE)	insulating
A0-T	1 ML Sr	TiO_2	-2.4	-0.3*	0.25 (MG)	0.8
A1-T	1 ML Sr, 1 ML O	TiO_2	-1.9	0.2*	0.08 (CBE)	1.3
C0-T	$\frac{1}{2}$ ML Sr, $\frac{1}{2}$ ML Si	TiO_2	-1.9	0.2*	0.31 (CBE)	1.0
B0-T	$\frac{1}{2}$ ML Sr	TiO_2	-1.6	0.5	0.15 (VBE)	1.0
B1-T	$\frac{1}{2}$ ML Sr, 1 ML O	TiO_2	-0.9	1.2	0.07 (VBE)	1.1
B2-T	$\frac{1}{2}$ ML Sr, $\frac{3}{2}$ ML O	TiO_2	-0.7	1.4	0.00 (VBE)	insulating
	reference supercell T	TiO_2	-0.6	1.5	0.00 (MG)	insulating
D0-S	1 ML Ti	SrO	-2.3	-0.2*	0.21 (CBE)	1.2
D1-S	1 ML Ti, 1 ML O	SrO	-2.1	0.0*	0.13 (CBE)	0.9
D2-S	1 ML Ti + $\frac{3}{2}$ ML O	SrO	-2.1	0.0*	0.10 (CBE)	1.0
D3-S	1 ML Ti + 2 ML O	SrO	-2.1	0.0*	0.30 (MG)	0.7
F0-S	$\frac{1}{2}$ ML Ti + $\frac{1}{2}$ ML Si	SrO	-2.3	-0.2*	0.11 (CBE)	0.7
E0-S	$\frac{1}{2}$ ML Ti	SrO	-0.9	1.2	0.37 (MG)	0.2
E1-S	$\frac{1}{2}$ ML Ti + 1 ML O	SrO	-0.8	1.3	0.46 (CBE)	0.3
E2-S	$\frac{1}{2}$ ML Ti + $\frac{3}{2}$ ML O	SrO	-0.7	1.4	0.47 (CBE)	0.3

As recently discussed in Ref.[12], we predict that structure A0-T is the experimentally realized structure. Although the band-offsets alone are not sufficient to identify the experimental interface structure, comparison with Table III shows that the experimental results are consistent with those of the A0-T interface composition, agreeing in the value of the VBE, the sign of the CBE, and the trend in the offsets with increasing oxygen pressure (*i.e.*, difference between A1-T and A0-T).

B. Fermi level pinning

The data in Table III indicate that the Fermi level is pinned to the conduction band edge in the $SrTiO_3$ in the presence of a full ML of cations in the interface layer. We observe such Fermi level pinning whether the cations at the interface are Sr, Ti, or a mix of Sr, Ti, and/or Si; furthermore, this behavior is also independent of the oxygen composition of the interface layer and the composition of the adjacent oxide plane. It is not *a priori* clear whether the pinning of the Fermi level in systems with a full ML of cations in the interface layer is physically meaningful or merely an artifact of the DFT band gap underestimation[32]. In this section, we verify that the Fermi level pinning is not a spurious effect. To do so, we use the GGA+Ua method to apply a Hubbard U correction[33] to the Ti d states (from which the conduction band edge in $SrTiO_3$ is composed) and the Si p states (which form the valence band maximum of Si) to independently increase the band gap of $SrTiO_3$ and shift the band edge of Si.

Fig. 9a shows the DOS of a heterostructure with interface A0-T as a function of the U applied to Ti d states. The band gap in the $SrTiO_3$ increases with increasing U, but the Fermi level remains pinned to the conduction band edge

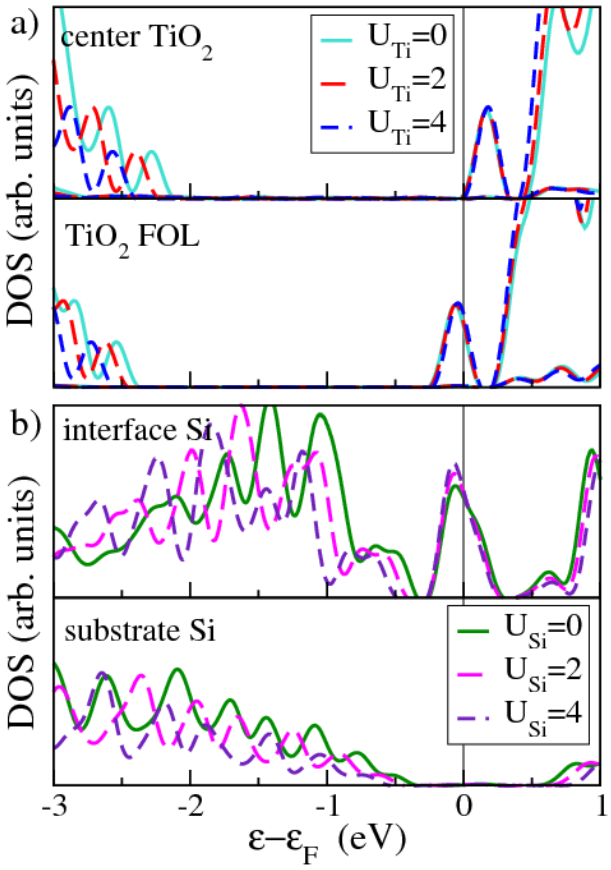

FIG. 9: Atom-projected DOS in TiO_2 (summed over the relevant Ti and O DOS) and Si layers in structure A0-T as a function of the Hubbard U applied to the a) Ti d-orbitals or the b) Si p-orbitals, showing that the Fermi level is pinned to the conduction band edge by the interface states.

in the $SrTiO_3$ due to the presence of partially filled states within the band gaps of both materials that are spatially localized at the interface ("interface states"). The properties of the interface states, which are derived from hybrid Si/Sr orbitals, are discussed below.

Figure 9b demonstrates that the conduction band edge of the silicon is also pinned at the interface for structure A0-T. Application of a range of U values to the Si p orbitals increases the Si band gap does not change the position of the Si conduction band edge with respect to the Fermi level; instead, the Si valence band edge shifts to lower energy values as U and the band gap increase.

Although one cannot use the LDA+U method within DFT to determine numerical values of band alignments, we believe that the behavioral trend observed with respect to the value of U in this case — i.e., that the Fermi level in structure A0-T is pinned regardless of the values of U, and thus the magnitude of the band gap — strongly suggests that the computed conduction band alignment and interface electronic structure are not spurious effects of the reduced DFT band gap. We also find this to be the case for the other interface compositions marked by a star in Table III. In addition, we confirm that the valence band offset remains constant with respect to U for several unpinned systems (*e.g.*, structures not labeled with a star in Table III), indicating that determining the conduction band offsets by adding the experimental gap to the valence band edge is a reasonable assumption for these systems.

C. Interface states and metallicity

All heterostructure compositions exhibit states unique to the interface region, primarily hybrid Si/Sr orbitals which are composed of a mix of Si dangling bond states and Sr s, p, and d-orbitals. Depending on the composition, other atoms in the interface region may also contribute to these states (*e.g.*, atoms in the FOL). The position and occupation of the states in the interface region determine whether the heterostructure is fully insulating or metallic. In all cases, both the silicon and the $SrTiO_3$ are insulating (*i.e.*, bulk-like) sufficiently far from the interface. Approximately 80%

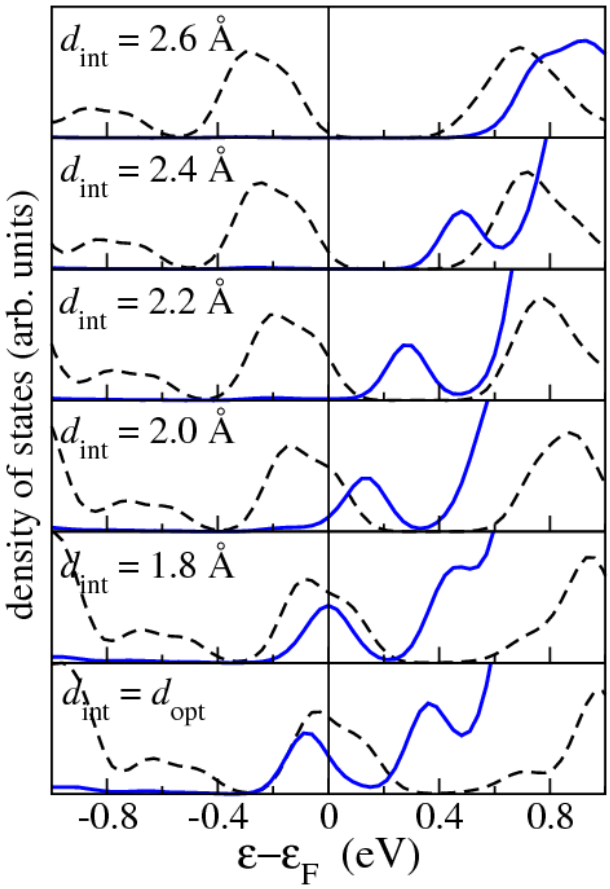

FIG. 10: Change in the occupation of the interfacial Ti d_{xy} (solid lines) and hybrid Si/Sr (dashed lines) states with the Ti-Si distance for the A0-T interface. The $SrTiO_3$ film is artificially fixed in a paraelectric state and the (fixed) TiO_2 distance is varied.

of the heterostructures studied are metallic, with partially filled states in the interface region. The length scale of the metallic region for each composition is given in Table III and illustrated qualitatively in the band diagrams in Figs. 2-5.

The character of the interfacial metallic states depends on the interface composition, as indicated in the band diagrams shown in Figs. 2-5. In most cases, the Si dangling bond states or states due to the hybridization of dangling bond states with Sr orbitals[8] overlap a band edge of the silicon substrate and become partially filled. These states extend over several atomic layers into the silicon substrate. For compositions in which silicon dimer formation at the interface is not energetically favored (*e.g.*, A0-S, A0-T, D0-S), the hybrid states are located within the silicon substrate band gap.

An additional contribution to interfacial metallic states can be present for heterostructures with a TiO_2 FOL. Due to the bonding geometry at the interface, these structures have a shorter Si-oxide separation ($d_{Si-oxide}$) than for a SrO FOL (see Sec. III). Consequently, the Ti-d_{xy} states (conduction band states) in the FOL have a significant spatial overlap with the hybrid Si/cation orbitals in the interfacial layer and the energies of the Ti d_{xy} states in the FOL are lowered with respect to that of the Ti d_{xy} states in $SrTiO_3$ planes further away from the interface. Thus electrons also transfer from the Si/cation orbitals into interface Ti d_{xy} states, as exemplified by the electron transfer shown in Fig. 8, giving rise to a metallic interface. The nature of the interaction is demonstrated in Fig. 10, which shows the DOS for interface A0-T as a function of $d_{Si-oxide}$: As $d_{Si-oxide}$ increases, the overlap decreases, the Ti orbitals shift upwards, and electrons return from the Ti d_{xy} states back to the hybrid Si/Sr states.

The behavior illustrated in Fig. 10 is similar to that of the $LaAlO_3/SrTiO_3$ heterointerface, arising from a similar chemical origin[34] and exhibiting a similar quasi-2D conducting electron gas at the interface. In the $SrTiO_3$/Si heterostructure, the electron gas decays perpendicular to the interface over the length of several $SrTiO_3$ unit cells ($\approx$1 nm). Similar to the $LaAlO_3/SrTiO_3$ system, we predict the occupation of these states can be modified via an electrical bias[35], as we discuss in more detail in Sec. VI E.

TABLE IV: $\Delta E_{\rm PE}$, the energy difference between the ground state and the paraelectric state for $SrTiO_3$ films with various geometry, film thickness, and lateral dimension of the supercell. For Au/$SrTiO_3$/Si heterostructures, which do not have a metastable paraelectric state, $\Delta E_{\rm PE}$ is the energy difference between a relaxed (polar) structure and its analogue computed with $\delta z_{\rm int}$ fixed to zero and all other atoms relaxed. For comparison, bulk $SrTiO_3$ under 1.7% in-plane compressive strain has a well-depth of 23 meV per perovskite unit cell. PE = paraelectric, FE = ferroelectric, MD=monodomain, SD=stripe multidomain. A polar ground state indicates that only a single metastable state exists.

geometry	film thickness (unit cells)	lateral width (unit cells)	ground state	maximum $\Delta E_{\rm PE}$ meV/2D cell
vacuum/$SrTiO_3$/vacuum	1-6	1	PE	(FE unstable)
Au/$SrTiO_3$/vacuum	1-6	1	PE	(FE unstable)
Au/$SrTiO_3$/Au	1-6	1	PE	(FE unstable)
vacuum/$SrTiO_3$/vacuum	1-6	2-6	FE, SD	-1
Au/$SrTiO_3$/vacuum	1-6	2-6	FE, SD	-30
Au/$SrTiO_3$/Au	1-3	2	FE, SD	-69
Au/$SrTiO_3$/Si (A0-T)	1-11	2	polar, MD	-600 (PE unstable)
Au/$SrTiO_3$/Si (B0-T)	1-9	2	polar, MD	-270 (PE unstable)
Au/$SrTiO_3$/Si (A0-S)	1-9	2	polar, MD	-370 (PE unstable)
Au/$SrTiO_3$/Si (B0-S)	1-9	2	polar, MD	-200 (PE unstable)

VI. FILM POLARIZATION

As reported in Ref.[1], the universal properties of the $SrTiO_3$/Si interface stabilize a positively poled state and inhibit ferroelectricity, preventing the formation of stable paraelectric (non-polar) or multidomain states. In the following subsections, we describe in detail the coupling between the interface and the film polarization. We also discuss the extent to which the interface composition influences the polarization behavior.

A. Role of the interface energetics

Since bulk $SrTiO_3$ strained to the Si lattice is predicted to be ferroelectric[16], in principle one can envision that thin $SrTiO_3$ films, in particular those grown on a non-metallic substrate such as Si, will attempt to screen depolarizing fields by forming multi-domain ferroelectric structures. In practice, for the $SrTiO_3$/Si system this is highly unlikely due to a large difference in energy scales: As shown in Ref.[1] the ferroelectric double-well depth of a completely screened $SrTiO_3$ thin film is less then 0.1 eV/interfacial unit cell while the actual $SrTiO_3$/Si interface system has only a single well that is significantly deeper ($\sim$0.5 eV/interfacial cell) due to the strong interfacial bonding that takes place. Thus, we expect that the interfacial bonds dominate over any tendency of the $SrTiO_3$ thin film to become ferroelectric.

As a explicit verification, we perform first principles calculations on a variety of systems to check for the presence and stability of multi-domain ferroelectric states in the $SrTiO_3$ film. First, we simulate $SrTiO_3$ films in the absence of the Si substrate and with no electrodes present (vacuum/$SrTiO_3$/vacuum), with an electrode on one side (Au/$SrTiO_3$/vacuum) and with electrodes on both sides (Au/$SrTiO_3$/Au). Second, we add the Si substrate and simulate the heterostructure with and without a top electrode (vacuum/$SrTiO_3$/Si and Au/$SrTiO_3$/Si). The simulations use $SrTiO_3$ films between 1 and 6 unit cells thick, and the lateral sizes of the simulation cells range up to 6 unit cells which allows for mono-domain or multi-domain striped ferroelectric structures with domain widths of 1, 2, or 3 unit cells.

Without Si (vacuum/$SrTiO_3$/vacuum, Au/$SrTiO_3$/vacuum and Au/$SrTiO_3$/Au), multi-domain ferroelectric structures have the lowest energy. However, the tendency for multi-domain ferroelectricity is weak: we find that the energy of the multi-domain ferroelectric structures is at most 20 meV per $SrTiO_3$ perovskite unit cell lower than the non-ferroelectric non-polar structures. Since the bulk strained $SrTiO_3$ ferroelectric well depth is 23 meV/unit cell, this simply confirms that, at best, the $SrTiO_3$ film can gain this much energy by forming multi-domain structures.

When the Si substrate is present and the $SrTiO_3$/Si interfacial bonds are formed (vacuum/$SrTiO_3$/Si and Au/$SrTiO_3$/Si), the non-ferroelectric polar state that we describe in Ref.[1] is the most stable structure. Typically, its energy is 170-600 meV/perovskite 2D unit cell lower than the non-ferroelectric non-polar structure, an order of

magnitude larger than the bulk ferroelectric well depth. Equally crucial is the fact that both the multi-domain ferroelectric structures and the paraelectric structures are *mechanically unstable* when the Si substrate is present: For all compositions, $Au/SrTiO_3/Si$ heterostructures with initial paraelectric, negatively poled, or multidomain states relax directly to non-ferroelectric positively poled structures. In other words, the negatively poled and paraelectric states are not metastable. In addition, mapping out the energy versus polarization curve for several structures shows no evidence of any metastable states in addition to the ground state, as we previously showed for interface A0-T[1].

An estimate of the interface energetics can be obtained by fixing $\delta z_{\rm int}$ to zero and allowing all other atoms to relax; the energy difference, $\Delta E_{\rm PE}$, between this "paraelectric" state and the ground state for several interface compositions is found in Table IV. As the table shows, $\Delta E_{\rm PE}$ is at least an order of magnitude larger for $Au/SrTiO_3/Si$ films compared to $SrTiO_3$ film geometries without silicon. Consequently, the interface energetics dominate the behavior of the $Au/SrTiO_3/Si$ system, enforcing the single positively poled ground state. As the $SrTiO_3$ film thickness increases, the interface effect will be diluted, and eventually the film could in principle become ferroelectric if we assume (very unrealistically) that the in-plane strain does not relax. We consider such thickness dependent behavior further in Sec. VI D.

These results demonstrate that without Si the $SrTiO_3$ is weakly multi-domain ferroelectric but that it becomes robustly non-ferroelectric and polar in the presence of the Si substrate. The bonding energetics at the $SrTiO_3/Si$ interface are an order of magnitude stronger than any tendency towards multi-domain ferroelectricity in the $SrTiO_3$ film. The interface dominates the behavior of the thin film heterostructure.

B. Role of the interface dipole and $\delta z_{\rm int}$

As discussed in Section IV B, the universal interface dipole induces a large, positive $\delta z_{\rm int}$ in the first oxide plane for all interface compositions. This displacement couples to the soft mode[36] in the $SrTiO_3$, so that the interface polarization propagates into the $SrTiO_3$ film. In addition to this mechanical coupling, the presence of the interface dipole creates a potential drop across the interface. Under short circuit conditions, the $SrTiO_3$ film polarizes in order to compensate for this voltage drop; due to the direction of the interface dipole, this requires a positive polarization. Thus, the chemically enforced electronic interface dipole creates both a mechanical and an electrical bias favoring a net positive polarization in the $SrTiO_3$ film.

The contribution of $\delta z_{\rm int}$ to the polarization can be described as the presence of a fixed boundary condition at the $SrTiO_3/Si$ interface. The relative contribution of the interface dipole is best illustrated by its removal: We perform a DFT calculation in which $\delta z_{\rm int}$ is fixed to its ground state value, but the silicon substrate and the $SrTiO_3$ film are separated by $\approx$10 Å. This removes the chemical bonds between the two, and, as the interface dipole is directly correlated to the interfacial chemical bonds, effectively removes the interface dipole while retaining all other system parameters. After relaxing all but the interface atoms, we compute the polarization of the test system. We find that the average polarization in the $SrTiO_3$ decreases by about half for 3-unit-cell-thick films with three different interface compositions (A0-T, A0-S, and B1-T), demonstrating that the interface dipole plays a key role in stabilizing the polarization.

C. Polarization profiles

In addition to governing the polarization direction, the $SrTiO_3/Si$ interface also affects the polarization profile through the $SrTiO_3$ film. As Fig. 11 shows, the polarization profile δz in the $SrTiO_3$ film is inhomogeneous for all interface compositions. This behavior is primarily a result of the large magnitude of the cation-anion displacement in the FOL.

If mobile screening charges are present, δz tends to decay toward the bulk value away from the interface in structures with $\delta z_{\rm int} > \delta z_{\rm bulk}$; if no screening charges are present, then the polarization decreases more rapidly as one moves from the $SrTiO_3/Si$ interface toward the electrode. The decay length is determined by the bulk materials properties of the oxide (*i.e.*, the cost of having a polarization gradient). In contrast, the net polarization (the average value of δz) is determined primarily by the chemical and electrostatic boundary conditions (*i.e.*, the interface composition). Fig. 11 illustrates the effect of the interface composition on the polarization profile for 3-unit-cell-thick $Au/SrTiO_3/Si$ films.

Due to the underlying 2×1 silicon surface reconstruction that is retained for some interface compositions (see Table I), the polarization can also be inhomogeneous in the plane. This is most evident for structures with 1/2 ML Sr at the interface. In these structures, as the induced charge density plots in Figs. 6 and 7show, the interface dipole — and thus the large cation-anion displacement in the FOL — is localized in one out of every two unit cells along the x-direction. The cation-anion displacement in the FOL is always smaller in the $SrTiO_3$ unit cell directly above

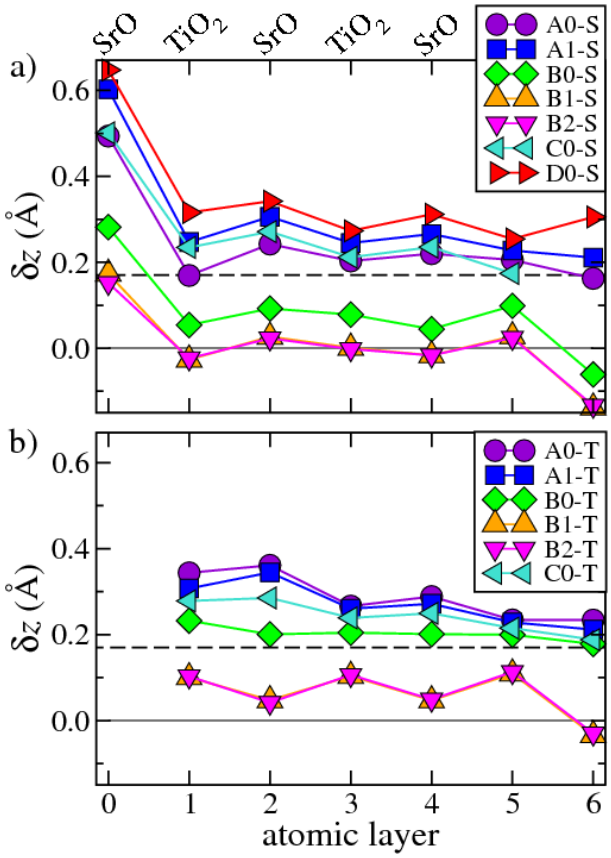

FIG. 11: Polarization profiles δz (cation-anion separation) for 3-unit-cell-thick films with different interface compositions. Compositions with a SrO and TiO_2 FOL are shown in a) and b), respectively. The dashed horizontal lines show the computed value for strained bulk $SrTiO_3$ (δz_{bulk}).

the silicon dimer, resulting in a smaller net polarization compared to interface compositions with a higher density of interfacial cations. After ≈2 unit cells away from the interface, the polarization in each plane becomes homogeneous; within the first two unit cells, the film can be thought of as bi-domain, corresponding to alternating Ti displacements with the 2×1 periodicity of the interface. However, the polarization does not cancel out due to the net interface dipole, leaving a small net positive polarization.

D. $SrTiO_3$ film thickness dependence

Figure 12 shows the computed cation-anion displacements in films of varying thickness for heterostructures with three different interface compositions. As the figure shows, δz_{int} is independent of the film thickness, but the average displacement is not. The figure also shows that δz asymptotes to a finite positive value away from the interface, indicating that the polarization charge is fully (a,b) or at least partially (c) screened in these structures. Interestingly, this causes the net polarization to initially *decrease* with increasing film thickness, often from a value significantly larger than the bulk value. This is in contrast to the behavior of canonical ferroelectric thin films[37], although polarization enhancement on a smaller scale has recently been predicted in some systems as a result of metal/oxide interface interactions[38,39]. The origins of this behavior in the $SrTiO_3$/Si system are discussed in more detail in the following sections.

E. Role of the top electrode

We investigate the effect of the top electrode on the polarization behavior by performing computations with various electrode materials. Changing the electrode work function changes the built-in bias across the $SrTiO_3$ film due to the

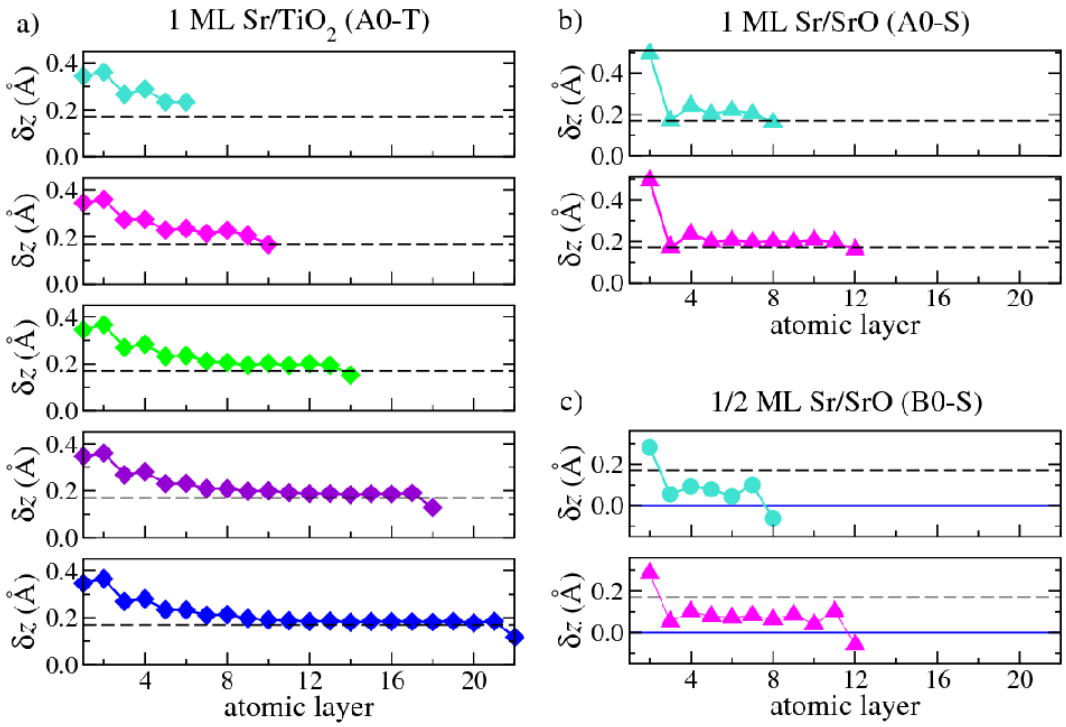

FIG. 12: DFT-computed displacements δz for each $SrTiO_3$ atomic plane in $Au/SrTiO_3/Si$ heterostructures of varying thickness with the a) A0-T, b) A0-S, and c) B0-S interface compositions. For reference, the computed bulk δz is given by the black dashed line; δz=0 is marked by the horizontal blue line in (c).

potential difference between the electrode and the Si substrate. Increasing the work function generally results in an increase in the net polarization, $\bar{P}$, as illustrated for interface A0-T in Fig. 13a. However, the interface polarization (or $\delta z_{\rm int}$) remains constant regardless of the strength of the perturbation to the system. The data in Fig. 13a emphasize the fact that $\delta z_{\rm int}$ is a fixed structural property of the interface.

Most strikingly, while a high density of surface oxygen vacancies will stabilize a negative polarization in ferroelectric thin films on a metallic substrate[6], this perturbation is not sufficient to switch the polarization at the $SrTiO_3/Si$ interface. In other words, our computations show that it is more favorable to form an energetically costly head-to-head domain wall than a negative polarization in the FOL. The head-to-head domain wall induced by surface oxygen vacancies is illustrated in Fig. 14; the figure also shows the computed displacements for films of various thickness with a monolayer of oxygen vacancies at the surface.

Figure 13b illustrates the relative insensitivity of the interface cation-oxygen displacement to the top electrode for all interface compositions. Plotting $\delta z_{\rm int}$ for films with a top gold electrode versus the same films without a top electrode (*i.e.*, vacuum termination) yields a linear function with a slope of close to unity. As the figure shows, the values of $\delta z_{\rm int}$ are generally larger by 0.05-0.1 Å when the gold electrode is present, indicating the additional bias due to the work function difference between the silicon substrate and the electrode. The range of the shift is correlated with the presence of interface states; the interface displacement increases more when electrons can transfer from the interface states to the electrode, thereby screening a larger net polarization charge. However, the figure illustrates that the bias due to the top electrode is not the dominant effect; the interface displacement/polarization is a structural feature that in some cases can be slightly enhanced by application of a bias field.

F. Role of screening by interface states

As noted in the previous section, the presence of partially occupied interface states can help screen the depolarizing field, stabilizing a larger net polarization. For example, examination of Table III shows that interfaces B1-S and B2-S, which have the smallest net polarizations, are fully insulating, with no partially filled interface states. In contrast, heterostructures with Ti in the interface layer — which tend to have a larger density of interface states than their counterparts with Sr interfacial cations (see Fig. 4 and Table III) — exhibit a larger net polarization. The presence of interface states alone is not necessary or sufficient to stabilize the film polarization, however; as Tables III and

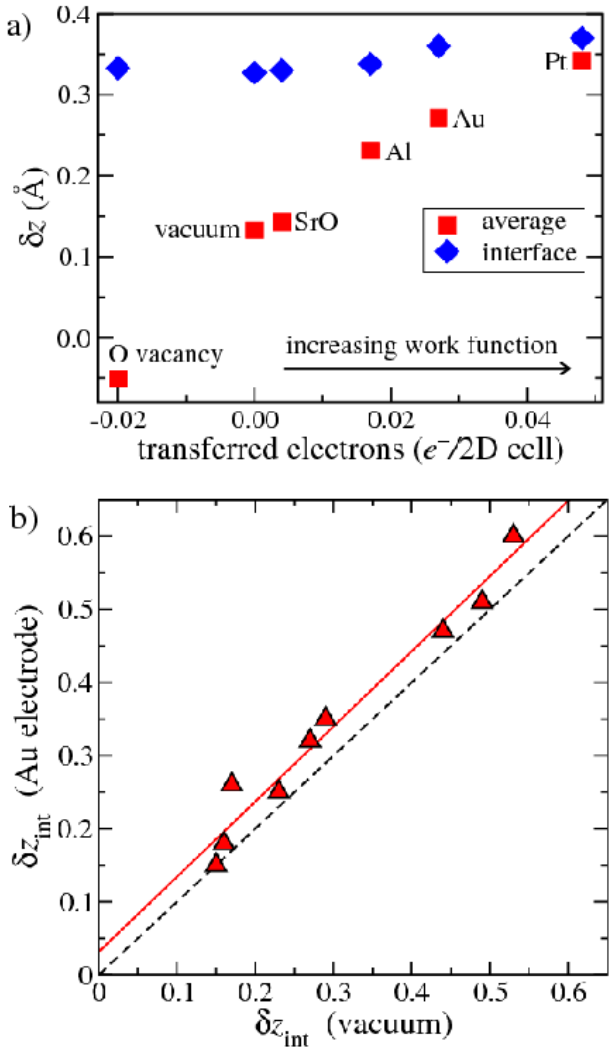

FIG. 13: a) δz of the interface and the film (averaged) as a function of metal electrode for interface A0-T. b) Interfacial $\delta z_{\rm int}$ for heterostructures with a top gold electrode vs $\delta z_{\rm int}$ for the same heterostructures without a top electrode (vacuum) for a range of interface compositions. The solid red line is a fit to the data; the dashed black line is of unit slope and zero intercept.

II demonstrate, interface compositions without interface states may also have a net positive polarization due to the additional role of the interface dipole, as discussed above.

VII. ELECTROSTATIC MODEL

In this section, we develop a continuous electrostatic model to further elucidate the relative contributions of the interface dipole, the fixed interface polarization, and mobile charge screening. In addition, we apply the model to predict the thickness dependent behavior of the polarization in $SrTiO_3$/Si heterostructures and to determine whether a "critical thickness" for the onset of ferroelectric behavior exists for these systems.

A. Model construction

The basic setup and key charge distributions for the film geometry are shown schematically in Fig 15, where the dipoles are approximated as infinite charged sheets separated by well defined distances. The sheet densities $+\sigma_{\rm int}$ and $-\sigma_{\rm int}$, separated by $d_{\rm int}$, represent the interface dipole, $p_{\rm int}$, and result in a potential drop across the interface, $\Delta V_{\rm int} = d_{\rm int}\sigma_{\rm int}/\epsilon_0$. The polarization in the $SrTiO_3$ film, which runs from $0 \leq z \leq l$, is represented by equivalent

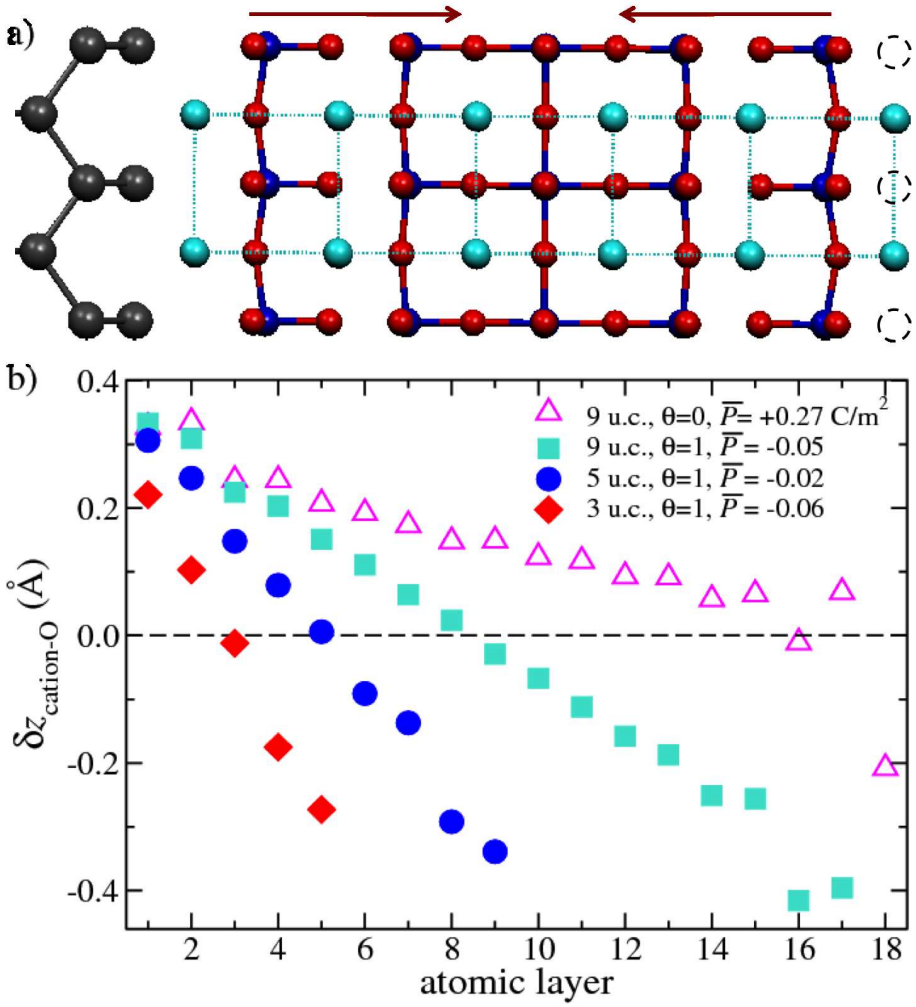

FIG. 14: a) DFT-computed atomic structure for a 5-unit-cell-thick $SrTiO_3$ film with one oxygen vacancy (dashed cirles) per surface unit cell. The high oxygen vacancy coverage stabilizes a head-to-head domain in the center of the $SrTiO_3$ film, with a positive interface polarization and a negative surface polarization, as indicated by the red arrows. Si, Sr, Ti, and O are grey, cyan, blue, and red, respectively. b) Cation-O displacements for $SrTiO_3$/Si films of various thickness with one oxygen vacancy per unit cell (θ=1) at the surface. For comparison, the triangles show the displacements in the 9-unit-cell-thick $SrTiO_3$/Si film with no oxygen vacancies (θ=0) and no top electrode.

surface charges $\pm\bar{P} = (1/l)\int_0^l P(z)dz$ at the two surfaces of the $SrTiO_3$ film (we consider the case of explicitly varying $P(z)$ immediately below), leading to a potential difference of $\bar{P}l$ across the film. Finally, if partially filled interface states are available, electron transfer across the $SrTiO_3$ film leads to screening sheet charges $\pm\sigma_s$ at the $SrTiO_3$/Si and the $SrTiO_3$/electrode interfaces, resulting in a potential drop of $\sigma_s(d_{\text{int}}+l+\lambda)$ across the film plus the interface region. Here, the screening charge is assumed to be localized in interface states at the Si/interface boundary, a distance of d_{int} away from the first oxide layer, while σ_s is located a distance λ (the characteristic screening length of the electrode material) into the electrode from the top $SrTiO_3$ plane.

The only free (mobile) charges in the system are $\pm\sigma_s$. Since the sheet charges $\pm\sigma_{\text{int}}$ are located outside the body of the film and D=0 inside both the Si substrate and the electrode, direct integration of the Maxwell equation gives $D(z) = \sigma_s/\epsilon_0$ and

$$E(z) = (\sigma_s - P(z))/\epsilon_0 \tag{3}$$

in the $SrTiO_3$ film. Assuming that both the silicon substrate and the gold electrode are thick enough to become bulk-like away from the interfaces, the potential drop across the system under short circuit boundary conditions is $\Delta V = \phi_{\text{Au}} - \chi_{\text{Si}}$, where ϕ_{Au} and χ_{Si} are the work function and electron affinity of the Au electrode and the Si substrate, respectively. We can thus write

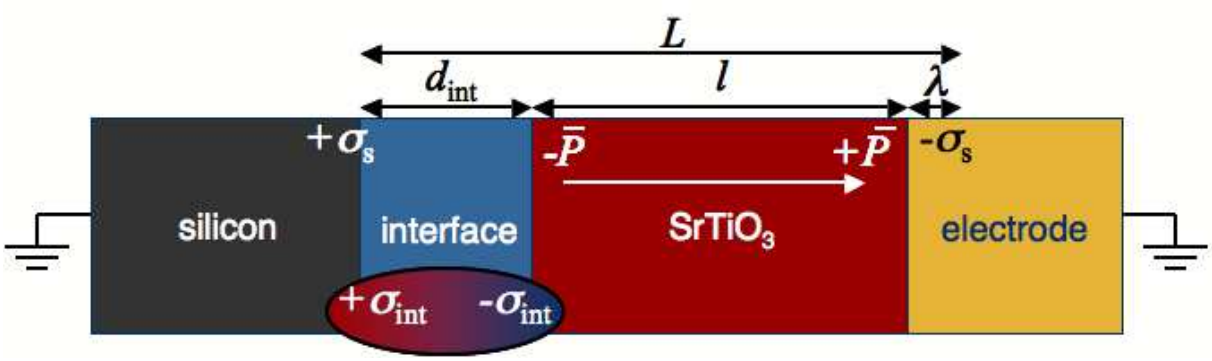

FIG. 15: Schematic of the relevant charges in the $Au/SrTiO_3/Si$ system.

TABLE V: Landau coefficients for bulk $SrTiO_3$ under 1.7% compressive strain (determined from GGA calculations).

A (Jm/C^2)	B (Jm^5/C^4)	C (Jm^9/C^6)	g (Jm^3C^2)
-1.31×10^9	-9.89×10^9	2.36×10^11	2.38×10^{-8}

$$\Delta V = \phi_{\rm Au} - \chi_{\rm Si} = \frac{1}{\epsilon_0}(\sigma_{\rm s} L - \bar{P} l) + \Delta V_{\rm int} \tag{4}$$

where $\bar{P} = (1/l)\int_0^l P(z)dz$ is the average film polarization and $L = d_{\rm int} + l + \lambda$. Solving for $\sigma_{\rm s}$ and substituting into Eq. 3 yields an expression for the electric field in the $SrTiO_3$ film:

$$E(z) = -\frac{1}{\epsilon_0}\left(P(z) - \frac{l}{L}\bar{P}\right) - \frac{1}{L}\left(\Delta V_{\rm int} - \Delta V\right), \tag{5}$$

where $\Delta V = \phi_{\rm Au} - \chi_{\rm Si}$. The first terms in Eq. 5 gives the depolarizing field resulting from incomplete charge compensation, as well as spatial variation or non-uniformity in $P(z)$. For thick films ($l \gg \lambda + d_{\rm int}$), this contribution goes to zero, as expected[40], (*i.e.*, for a sufficiently thick film, surface/interface effects are negligible). The second term combines the electrical bias due to the asymmetric electrodes with that due to the interface potential drop; this term also goes to zero as $l \to \infty$.

With this simplified expression for the field through the $SrTiO_3$, we can now use a Landau-Ginzburg-Devonshire (LGD) model to determine the minimum energy film polarization profile $P(z)$ for a given film thickness. Within LGD, the free energy (per unit cell) of the thin film is

$$F[P(z)] = F_0 + \int_0^l dz \left(\frac{1}{2}AP(z)^2 + \frac{1}{4}BP(z)^4 + \frac{1}{6}CP(z)^6 + \frac{1}{2}g\left(\frac{dP}{dz}\right)^2 - \frac{1}{2}E(z)P(z)\right), \tag{6}$$

where F_0 is the free energy of the paraelectric state, and the standard coefficients A, B, and C are determined by fitting to the computed energy versus polarization curve of bulk strained $SrTiO_3$. The coefficient g of the gradient term is obtained by determining the total energy difference between the bulk ferroelectric phase and bulk $SrTiO_3$ with an imposed long wavelength polarization gradient $P(z) = P_{\rm bulk}\cos(2\pi z/L)$. We have used $L = 10a$, where a is the lattice constant of bulk strained $SrTiO_3$. The values of the Landau coefficients are given in Table V.

The polarization profile, $P(z)$, is found by minimizing $F[P(z)]$ with respect to $P(z)$ and numerically solving the resulting second-order differential equation subject to the boundary conditions $P(0) = P_{\rm int}$ and $P(l) = a\bar{P}^2 + b\bar{P} + c$. The former boundary condition is the fixed interface polarization determined from DFT calculations[42]; the latter is determined empirically from our database of $SrTiO_3/Si$/electrode and electrode/$SrTiO_3$/electrode film calculations, shown in Fig. 16. The coefficients a, b, and c are constants related to the materials forming the interface. For

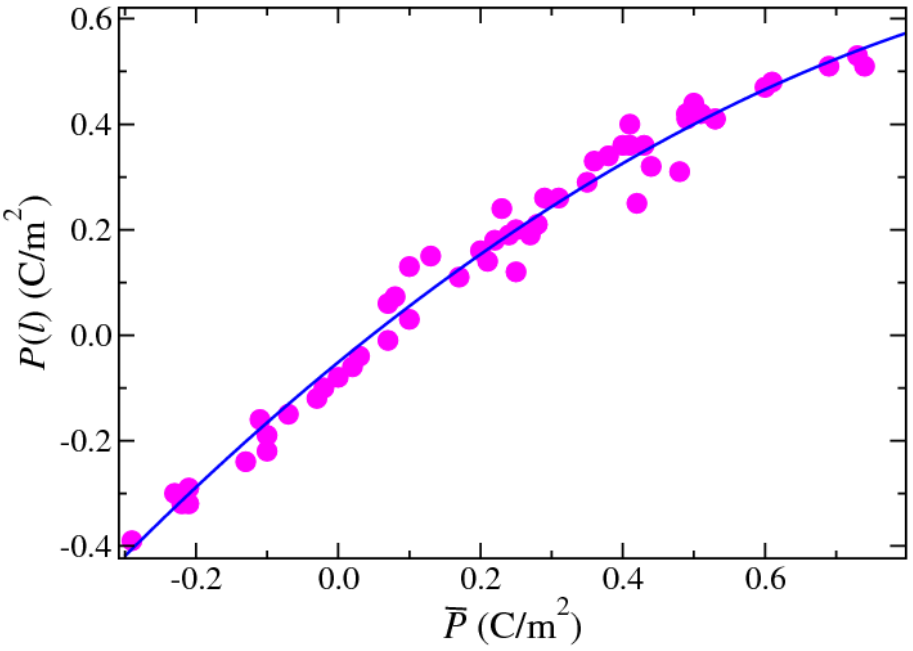

FIG. 16: $P(l)$ from first-principles DFT calculations for $SrTiO_3$ films with a SrO-termination and a gold electrode. Each data point corresponds to a system with a different $SrTiO_3$/Si interface structure and/or a different film thickness. Also included are points for Au/$SrTiO_3$/Au films of various thickness. The data is fit to determine the expression for the boundary condition $P(l)$.

example, with a gold electrode and a SrO-terminated[43] $SrTiO_3$ film, $P(l) = a\bar{P}^2 + b\bar{P} + c$, where a=-0.40 m^2/C, b=1.10 (unitless), and c=-0.05 C/m^2.

The only unknown parameter in Eq. 6 is $\bar{P}$. Therefore, the solution $P(z)$ to the boundary value problem is found for a range of input $\bar{P}$, then substituted into Eq. 6 to determine the value of $\bar{P}$ that minimizes the energy. As Fig. 17a shows, the $P(z)$ curves obtained in this way (solid lines) are in good agreement with the DFT data (symbols).

B. Application 1: Separating interface contributions

We now use the model to examine the relative effects of the fixed interface polarization, the interface dipole, and polarization screening via interface states. Figure 17a shows the LGD polarization profile across a 9-unit-cell-thick film under various conditions. First, including the presence of the interface dipole ($\Delta V_{\rm int}$), the screening charge ($\sigma_{\rm s}$), and the interface polarization ($P_{\rm int}$) using parameters from DFT for the A0-T interface composition yields the blue curve in Fig. 17a. The model is in good agreement with the DFT data (blue circles; see Ref. 40), with the polarization asymptoting to the bulk strained $SrTiO_3$ value away from the interface, indicating full polarization charge compensation. Removing the contribution due to mobile charge screening by setting $\sigma_{\rm s}$ =0 to model a heterostructure without interface states and/or a top electrode, causes $P(z)$ to decrease to a smaller, but non-zero value away from the interface (cyan curve). This case, which agrees well with the DFT-computed polarization for the A0-T heterostructure in which the Au electrode is replaced by vacuum (cyan diamonds) to remove screening effects, demonstrates the stabilizing effect of the interface dipole on the film polarization. This is further emphasized by setting both $\sigma_{\rm s}$ and $\Delta V_{\rm int}$ to zero to simulate a heterostructure lacking both interface states and an interface dipole. As illustrated by the magenta curve in Fig. 17a, neglecting both effects results in a rapid decrease of $P(z)$ to zero away from the interface. (Removing the constraint of a fixed interface polarization in addition gives $P(z) = 0$.)

C. Application 2: Predicting the thickness dependence

We also apply the model to determine the thickness-dependent behavior of the system for films inaccessible to DFT due to computational expense. Figure 17b compares the average polarization for monodomain situations as a function of $SrTiO_3$ film thickness for Au/$SrTiO_3$/Si heterostructures with several different interface compositions.

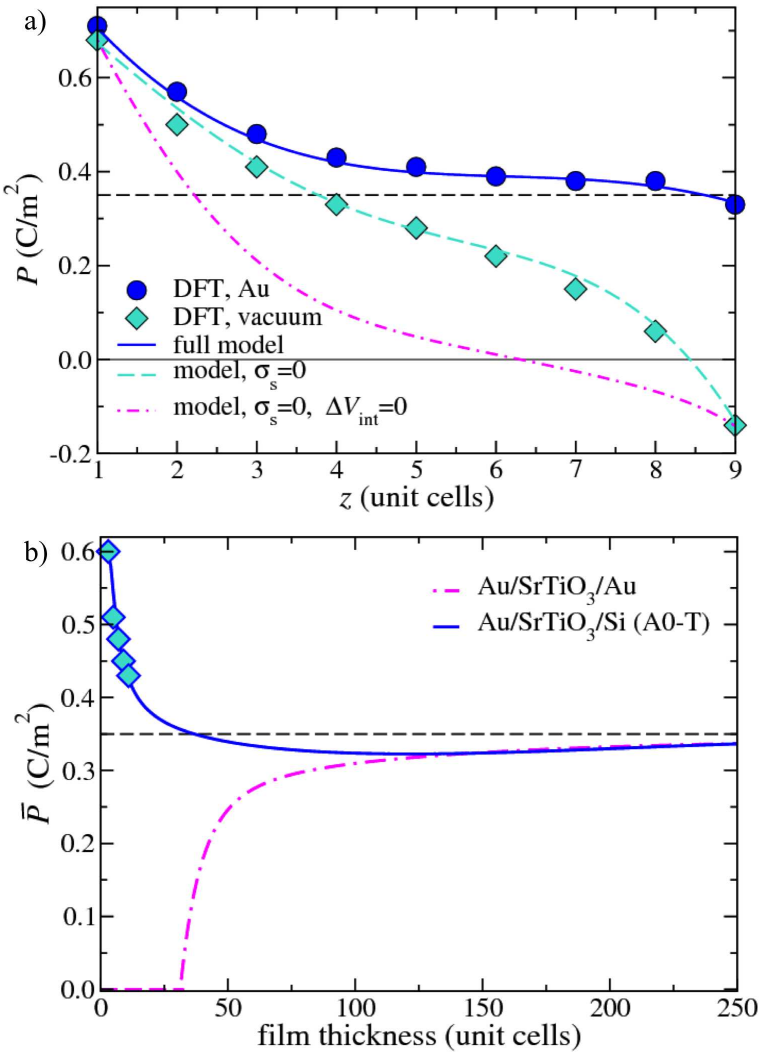

FIG. 17: a) Comparison of polarization profiles obtained via DFT and the model, illustrating the different contributions from the terms in Eq. 5 (see text). b) Average monodomain polarization as a function of film thickness for $Au/SrTiO_3/Si$ heterostructures with the A0-T interface composition. Results for $Au/SrTiO_3/Au$ are shown for comparison. Solid lines are results from the model; symbols indicate DFT-computed values. The horizontal dashed lines indicate the bulk value.

The figure also shows the thickness dependence of a monodomain $Au/SrTiO_3/Au$ capacitor structure (*i.e.*, both top and bottom boundary conditions from Fig. 16, and no bias terms in E). Interestingly, in addition to fixing the polarization direction, the interface has a profound effect on the thickness-dependent behavior: the net polarization in $Au/SrTiO_3/Si$ films decreases with increases film thickness from a large positive value in 3-unit-cell-thick films. This behavior, which is fundamentally different to that of polarization versus thickness in a prototypical capacitor structure such as $Au/SrTiO_3/Au$, arises from the large, structurally-induced interface polarization. As the film is thickened, the net polarization asymptotes to P_{bulk} regardless of the substrate. The model predicts that in the absence of strain relaxation (*i.e.*, a purely theoretical situation), the behavior of $Au/SrTiO_3/Si$ would become indistinguishable from that of $Au/SrTiO_3/Au$ for $SrTiO_3$ films thicker than about 120 unit cells (≈50 nm).

D. Application 3: "Critical thickness" for monodomain ferroelectricity

We now use the above model to examine the possibility of ferroelectric switching in thicker films and to predict the critical thickness at which the interface no longer dominates the heterostructure behavior. Under the assumption that the interface polarization is fixed — a good assumption as we find no evidence of metastable negatively poled interface state for films of any composition or thickness — the film must form a 180° head-to-head domain wall in order to

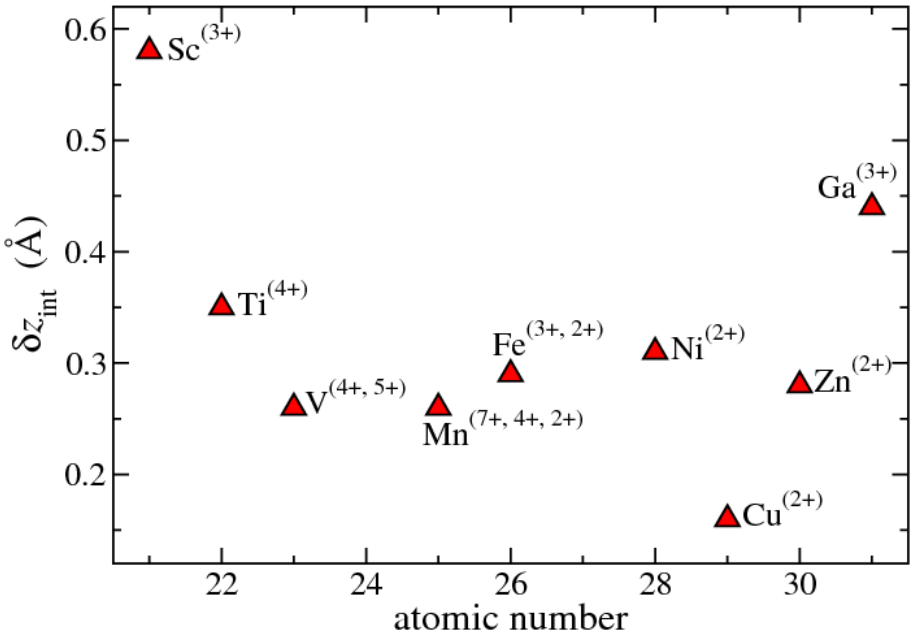

FIG. 18: δz_{int} for $SrTiO_3$/Si heterostructures with modified A0-T interface compositions in which the Ti in the FOL is replaced by various transition metal cations. The most common oxidation state(s) of each substitutional cation is shown in parentheses.

have a net negative polarization (or to have alternating net negative and net positive stripes). Thus, to determine the critical thickness, l_{crit}, at which ferroelectric switching can first occur, we find the minimum film thickness that can support a stable 180° head-to-head domain configuration in a Au/$SrTiO_3$/Si heterostructure. We use the above LGD theory to determine $P(z)$ for films of varying thickness, l, with the boundary conditions $P(0) = P_{\text{int}}$ and $P(l) = -P_{\text{bulk}}$. The smallest l for which $F[P(z)] < 0$ corresponds to l_{crit}.

We perform this analysis with values of P_{int} and ΔV_{int} obtained from our DFT calculations of heterostructures with several different interface compositions. We find that $l_{\text{crit}} \approx$20 nm or about 50 unit cells. This value is insensitive to the interface composition, varying on the order of 1-2 unit cells over the range of compositions studied. As $SrTiO_3$ films of such thickness are no longer under compressive strain when grown epitaxially on silicon[7] — and therefore not ferroelectric — our model predicts that ferroelectric switching will not be observed in $SrTiO_3$/Si heterostructures, regardless of the interface composition. We note that this result assumes no mass ion motion (*e.g.*, reversible introduction/removal of oxygen vacancies or other defects). It is possible that such a mechanism is responsible for observations of piezo-force microscopy contrast in experiments[4] as discussed previously[1].

VIII. GENERALIZATION TO OTHER HETEROSTRUCTURES

As discussed above, both the fixed boundary conditions and the interface dipole are fundamental characteristics of the $SrTiO_3$/Si interface, observed for all interface compositions, and as a result, ferroelectric switching of the polarization between monodomain states is prevented for any interface composition. Consideration of the physical/chemical interactions leading to these properties suggests that we can generalize this result even further to encompass all perovskite oxide/non-polar semiconductor heterostructures. To test this hypothesis, we replace the $SrTiO_3$ film with either $BaTiO_3$ or $PbTiO_3$ in heterostructures with two different interface compositions: A0-T (the predicted $SrTiO_3$/Si interface structure[1]) and B1-S (the predicted BaO/Si interface structure[23]).

We find that, as with the $SrTiO_3$/Si heterostructures discussed above, $BaTiO_3$/Si and $PbTiO_3$/Si heterostructures have a large positive interface polarization and a net positive film polarization, and further, do not have a metastable negatively poled state for either interface composition. Fixing the interface displacement to zero and relaxing the other atoms in a 3-unit-cell-thick film gives an energy difference of 0.7 (1.2) eV/2D cell between the ground and "paraelectric" states of a $BaTiO_3$ ($PbTiO_3$) heterostructure with the A0-T interface composition, similar to the value of 1.2 eV/2D cell computed for the analogous $SrTiO_3$ heterostructure (Table IV).

We also observe that changing the charge state of the interface via substitution of either the Sr and/or Ti cations is insufficient to change the interface properties. For example, replacing the Ti cations in the FOL with transition metal cations of various oxidation states does not stabilize a negatively poled state in 3-unit-cell-thick films. In addition,

the interface cation-oxygen displacement remains large and positive regardless of the oxidation state of the transition metal cation in the FOL, as demonstrated in Fig. 18. Similarly, substitution of cations of different valency for the interfacial Sr cations also fails to qualitatively change the interfacial boundary conditions. These results provide further evidence that the interface behavior is largely driven by the high oxygen electronegativity, leading to a net electron transfer from the semiconductor to the oxide side of the interface. We therefore suggest that this feature is general to the class of perovskite oxide/non-polar semiconductor heterostructures.

IX. SUMMARY

In conclusion, we have performed first-principles computations to study the technologically important $SrTiO_3$/Si heterostructure and determine its behavior for a wide range of possible interface compositions. Our results show that the electronic properties such as interface metallicity and band alignment are very sensitive to the composition of the interface layer. We also demonstrated that the magnitude of the film polarization can also be tuned via the interface composition. However, we find that the fixed direction (and presence) of the polarization is a fundamental property independent of the interface composition, arising as a result of the abrupt covalent-to-ionic bonding transition across the interface which leads to strongly fixed chemo-mechanical and electrostatic boundary conditions.

We developed an electrostatic model to include these interface effects within a standard LGD framework, which we then used to predict the thickness dependent behavior of $SrTiO_3$/Si. In addition, we applied the model to examine the possibility of non-conventional ferroelectric switching via head-to-head domain formation. We demonstrated that the lower boundary for this phenomena to occur is ≈20 nm, much greater than the achievable thickness for coherent, strained $SrTiO_3$ films on silicon, and therefore not predicted to occur. Our results shed light on necessary properties for an interface that successfully couples ferroelectricity to silicon, as well as provide a fundamental understanding of forces that dominate the nanoscale behavior in this interesting class of heterointerfaces. Such understanding can aid in the interpretation of experimental data on these heterostructures and the prediction of the properties of other oxide/semiconductor heterostructures.

X. ACKNOWLEDGMENTS

We acknowledge support from the National Science Foundation under MRSEC DMR 0520495, as well as computational support from the NCSA TeraGrid and Yale High Performance Computing. This work was supported in part by the facilities and staff of the Yale University Faculty of Arts and Sciences High Performance Computing Center and by the National Science Foundation under grant #CNS 08-21132 that partially funded acquisition of the facilities. We thank J.W. Reiner, F.J. Walker, and C.H. Ahn for insightful discussions.

XI. APPENDIX: DETERMINATION OF THE BAND ALIGNMENT

We determine the band alignment across the $SrTiO_3$/Si interface for each interface composition in the following manner. First, using a windowing technique[41] to average out the oscillations due to the atomic nuclei, we find the macroscopic averaged electrostatic potential of the heterostructure along the direction perpendicular to the interface, $V(z)$. $V(z)$ gives the relative alignment of the internal potential in the silicon and the $SrTiO_3$ regions ($\Delta V_{\text{internal}}$).

The position-dependent $SrTiO_3$ valence band edge $E_V^{SrTiO_3}(z)$ is given by adding $V_0^{SrTiO_3}$ to $V(z)$ within the $SrTiO_3$ region of the heterostructure. Here $V_0^{SrTiO_3}$ is the energy difference between the valence band edge $E_V^{\text{bulk } SrTiO_3}$ and the average internal electrostatic potential $V_{\text{internal}}^{SrTiO_3}$ of bulk strained $SrTiO_3$. (We find $V_0^{SrTiO_3}$=6.3 eV for bulk $SrTiO_3$ under a biaxial compressive strain of 1.7%.) The position-dependent $SrTiO_3$ conduction band edge $E_C^{SrTiO_3}(z)$ is then determined by adding the experimental band gap $E_{g,\text{expt}}^{SrTiO_3}$=3.2 eV to $E_V^{SrTiO_3}$.

The position-dependent band edges in the Si region of the heterostructure ($E_V^{Si}(z)$ and $E_C^{Si}(z)$) are found in an analogous manner. (Our calculations give V_0^{Si}=4.0 eV, and we use $E_{g,\text{expt}}^{Si}$=1.12 eV.) The band offsets in the $SrTiO_3$/Si heterostructures are then determined by $\Delta E_V = E_V^{SrTiO_3}(z_1) - E_V^{Si}(z_2)$ and $\Delta E_C = E_C^{SrTiO_3}(z_1) - E_C^{Si}(z_2)$, where z_1 and z_2 indicate positions in the center of the $SrTiO_3$ and Si regions of the heterostructure, respectively. The resulting values of ΔE_V and ΔE_C are reported in Table III.

As discussed in Section V A, we also computed the electrostatic potential and band edges for a reference system composed of silicon and $SrTiO_3$ slabs separated by vacuum in the z-direction. This system describes the band alignment between $SrTiO_3$ and silicon in the absence of interface chemistry. We note that this alignment, illustrated in Fig. 19, depends on the surface termination of the $SrTiO_3$ slab, as indicated by the reference values in Table III:

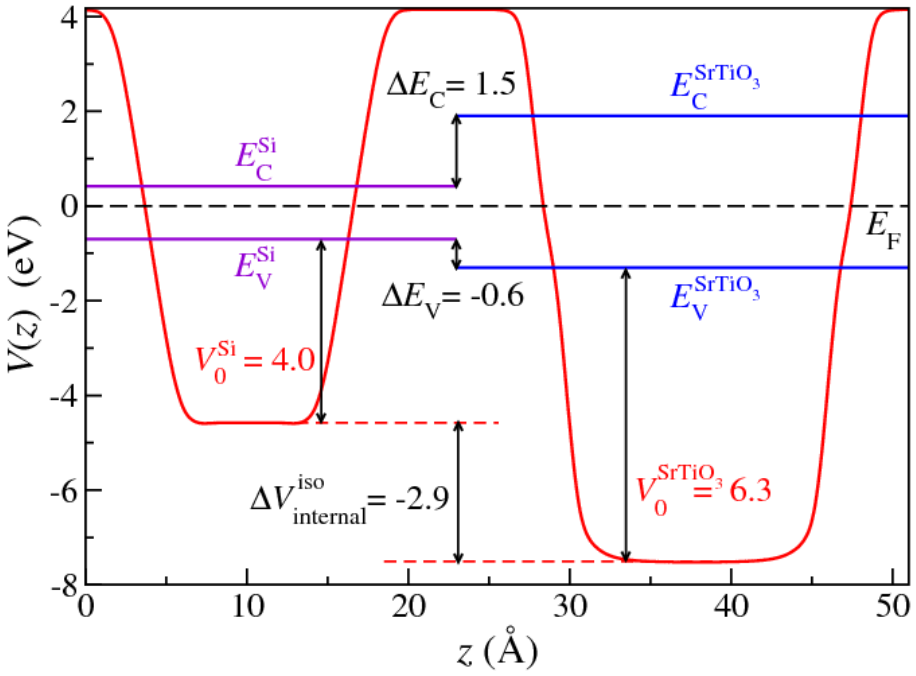

FIG. 19: Computed electrostatic potential (red curve) for isolated Si and $SrTiO_3$ slabs in the same DFT supercell illustrating the method for determining the reference band and internal potential alignments between bulk-like Si and $SrTiO_3$ (*i.e.*, in the absence of interfacial effects. The symmetric $SrTiO_3$ slab is terminated with TiO_2 planes and the silicon surface is compensated with hydrogen.

Along the (001) direction, the $SrTiO_3$ bulk can be terminated with either an SrO on a TiO_2 plane. The two $SrTiO_3$ surfaces are characterized by different electron affinities; the computed values in this study are 0.8 and 3.7 eV for SrO- and TiO_2-terminated surfaces, respectively. Consequently, the relative Fermi level positions and band alignments are also different, an important consideration when comparing the band offsets for heterostructures with different initial $SrTiO_3$ planes.

Finally, as mentioned above and discussed in Section V A, the conduction band edges are determined by adding the experimental band gaps to E_V in order to correct the well-known underestimation of the band gap in DFT[26]. Separately, we assume that DFT can accurately predict the valence band edges. We also require knowledge of the interface electronic structure; in particular, whether the Fermi energy is pinned by interface states or at the edge the conduction band on either side of the interface. Both situations occur within the set of $SrTiO_3$/Si interface compositions examined in this study, as discussed in Section V B. In these cases, noted by a * in Table III, the conduction band edges are determined from the computed atom-projected DOS, and the valence band edges are determined by subtraction of the relevant experimental band gap in order to obtain the valence band offset. As discussed in Section V A, both valence and conduction band edges can in principle shift with respect to LDA or GGA when a better description of exchange and correlation is employed. However, as demonstrated in Sec. V B, the pinning of the conduction band is independent of the band gap, and therefore we do not expect it to be affected by an improved band structure calculation.

[1] A. M. Kolpak, F. J. Walker, J. W. Reiner, Y. Segal, D. Su, M. S. Sawicki, C. C. Broadbridge, Z. Zhang, Y. Zhu, C. H. Ahn, et al., Phys. Rev. Lett. **105**, 217601 (2010).
[2] R. A. McKee, F. J. Walker, and M. F. Chrisholm, Phys. Rev. Lett. **81**, 3014 (1998).
[3] S. B. Mi, C. L. Jia, V. Vaithyanathan, L. Houben, J. Schubert, D. G. Schlom, and K. Urban, Appl. Phys. Lett. **93**, 101913 (2008).
[4] M. P. Warusawithana, C. Cen, C. R. Sleasman, J. C. Woicik, Y. Li, L. F. Kourkoutis, J. A. Klug, H. Li, P. Ryan, L.-P. Wang, et al., Science **324**, 367 (2009).
[5] R. Moos, W. Menesklou, and K. H. Hardtl, Appl. Phys. A **61**, 389 (1995).
[6] R. V. Wang, D. D. Fong, F. Jiang, M. J. Highland, P. H. Fuoss, C. Thompson, A. M. Kolpak, J. A. Eastman, S. K. Streiffer, A. M. Rappe, et al., Phys. Rev. Lett. **102**, 047606 (2009).

[7] J. C. Woicik, H. Li, P. Zschack, E. Karapetrova, P. Ryan, C. R. Ashman, and C. S. Hellberg, Phys. Rev. B **73**, 024112 (2006).
[8] K. Garrity and S. Ismail-Beigi, Phys. Rev. B **80**, 085306 (2009).
[9] C. J. Forst, C. R. Ashman, K. Schwarz, and P. E. Blochl, Nature **427**, 53 (2003).
[10] P. W. Peacock and J. Robertson, Appl. Phys. Lett. **83**, 5497 (2003).
[11] X. Zhang, A. A. Demkov, H. Li, X. Hu, Y. Wei, and J. Kulik, Phys. Rev. B **68**, 125323 (2003).
[12] A. M. Kolpak and S. Ismail-Beigi, Phys. Rev. B **83**, 165318 (2011).
[13] http://dcwww.camp.dtu.dk/campos/Dacapo/.
[14] D. Vanderbilt, Phys. Rev. B Rapid Comm. **41**, 7892 (1990).
[15] L. Bengtsson, Phys. Rev. B **59**, 12301 (1999).
[16] J. H. Haeni, P. Irvin, W. Chang, R. Uecker, P. Reiche, Y. L. Li, S. Choudhury, W. Tian, M. E. Hawley, B. Craigo, et al., Nature **430**, 758 (2004).
[17] R. A. McKee, F. J. Walker, M. Buongiorno Nardelli, W. A. Shelton, and G. M. Stocks, Science **300**, 1726 (2003).
[18] A. A. Demkov, L. R. C. Fonseca, E. Verret, J. Tomfohr, and O. F. Sankey, Phys. Rev. B **71**, 195306 (2005).
[19] F. Niu and B. W. Wessels, J. Crystal Growth **300**, 509 (2007).
[20] I. N. Yakovkin and M. Gutowski, Phys. Rev. B **70**, 165319 (2004).
[21] L. F. Kourkoutis, C. S. Hellberg, V. Vaithyanathan, H. Li, M. K. Parker, K. E. Andersen, D. G. Schlom, and D. A. Muller, Phys. Rev. Lett. **100**, 036101 (2008).
[22] I. Anisimov, F. Aryasetiawan, and A. I. Lichtenstein, J. Phys. Condens. Matter **9**, 797 (1997).
[23] Y. Segal, J. W. Reiner, A. M. Kolpak, Z. Zhang, S. Ismail-Beigi, C. H. Ahn, and F. J. Walker, Phys. Rev. Lett. **102**, 116101 (2009).
[24] J. W. Reiner, A. Posadas, M. Wang, T. P. Ma, and C. H. Ahn, Microelectron. Eng. **85**, 36 (2007).
[25] S. M. Sze and K. K. Ng, *Physics of Semiconductor Devices* (John Wiley & Sons, 2007).
[26] M. S. Hybertsen and S. G. Louie, Phys. Rev. Lett. **55**, 1418 (1985).
[27] R. W. Godby and L. J. Sham, Phys. Rev. B **40**, 1849 (1994).
[28] H.-P. Komsa, P. Broqvist, and A. Pasquarello, Phys. Rev. B **81**, 205118 (2010).
[29] F. Amy, A. S. Wan, A. Kahn, F. J. Walker, and R. A. McKee, J. Appl. Phys. **96**, 1635 (2004).
[30] S. A. Chambers, Y. Liang, Z. J. Yu, R. Droopad, J. Ramdani, J. M. Finder, and K. Eisenbeiser, J. Vac. Sci. Tech. A **19**, 934 (2001).
[31] S. A. Chambers, T. Droubay, T. C. Kaspar, and M. Gutowski, J. Vac. Sci. Technol. B **22**, 2205 (2004).
[32] C. S. Wang and W. E. Pickett, Phys. Rev. Lett. **51**, 597 (1983).
[33] V. I. Anisimov, J. Zaanen, and O. K. Andersen, Phys. Rev. B **44**, 943 (1991).
[34] H. Chen, A. M. Kolpak, and S. Ismail-Beigi, Phys. Rev. B **79**, 161402 (2009).
[35] C. Cen, S. Thiel, G. Hammerl, C. W. Schneider, K. E. Andersen, C. S. Hellberg, J. Mannhart, and J. Levy, Nat. Mater. **7**, 298 (2008).
[36] E. F. Steigmeier and H. Auderset, Solid State Commun. **12**, 565 (1973).
[37] J. Junquera and P. Ghosez, Nature **422**, 506 (2003).
[38] N. Sai, A. M. Kolpak, and A. M. Rappe, Phys. Rev. B Rapid Comm. **72**, 020101(R) (2005).
[39] M. Stengel, D. Vanderbilt, and N. A. Spaldin, Nat. Mater. **8**, 392 (2009).
[40] R. R. Mehta, B. D. Silverman, and J. T. Jacobs, J. Appl. Phys. **44**, 3379 (1973).
[41] A. Baldereschi, S. Baroni, and R. Resta, Phys. Rev. Lett. **61**, 734 (1988).
[42] The polarization in is estimated by multiplying $P_{\rm bulk}$ times the ratio of the cation-O displacement in a given SrO or TiO_2 layer relative to that in bulk strained $SrTiO_3$. Within GGA, $P_{\rm bulk}$ is computed by the Berry phase method to be 0.35 C/m^2 for bulk $SrTiO_3$ with -1.7% in-plane strain. The cation-O displacement in bulk strained $SrTiO_3$ is 0.17 Å.
[43] We focus on SrO-terminated films because STEM images show that the experimental films have Sr at the surface. Calculations with TiO_2-terminated films show the same qualitative behavior, but with different values of the coefficients describing the polarization at the $SrTiO_3$/electrode interface.